Electrocatalytic activity of symmetric and asymmetric Co(II) and Mn(III) porphyrins in the presence of graphene quantum dots towards the oxidation of hydrazine

Masters of Science

Of

Rhodes University

By

Mbulelo Jokazi

June 2022

Acknowledgements

I would like to show my appreciation to my supervisor, **Distinguished Professor Tebello Nyokong** for her patience and valuable feedback. The teachings and guidance through my Masters degree. Thank you very much Prof, for all the support I truly appreciate it.

A big thank you to my mentor Dr Lekhetho Mpeta for mentoring me and your generous support. I greatly appreciate all your effort. I am also grateful to Sixolile Centane, Reitumetse Nkhahle and Nobuhle Ndebele for their assistance throughout my research. A special thank you to Gail Cobus, Dr Jonathan Britton, Professor John Mack and everyone in lab S22.

I would also like to thank my parents Priscilla and Vuyisile Jokazi for their moral support and encouragement. Your prayers for me is what sustained me this far. My brother Sakhumzi Jokazi thank you for your continuous support.

I am also thankful to National Research Foundation (NRF) and Desmond Goddard (2021) for funding.

Lastly, I would like to thank God for guiding me through all the difficulties.

Abstract

The influence of metal porphyrins in electro-oxidation of hydrazine is explored. A series of symmetric and asymmetric porphyrins alone and in the presence of graphene quantum dots (GQDs) are employed in this work. Tetra 4-aminophenyl porphyrin, manganese tetra 4-aminophenyl porphyrin, manganese tetra 4-aminophenyl porphyrin--GQDs, and manganese tetra 4-aminophenyl porphyrin@GQDs are the symmetric porphyrins. The asymmetric porphyrin and composites are 5, 10, 15-tris(aminophenyl)-20-(4-carboxyphenyl) porphyrins, manganese 5, 10, 15-tris(aminophenyl)-20-(4-carboxyphenyl) porphyrins, cobalt 5, 10, 15-tris(aminophenyl)-20-(4-carboxyphenyl) porphyrins, manganese 5, 10, 15-tris(aminophenyl)-20-(4-carboxyphenyl) porphyrins--GQDs, and cobalt 5, 10, 15-tris(aminophenyl)-20-(4-carboxyphenyl) porphyrins--GQDs.

These complexes were synthesized and characterized accordingly and applied for electrocatalysis. The electrocatalytic experiments were carried out using glassy carbon electrode and the modification was through drop-dry method. The porphyrin and GQDs synthesized were characterized using UV-Vis spectroscopy, Mass spectrometry, X-ray diffraction, transmission electron microscopy, X-ray photoelectron spectroscopy and energy dispersive x-ray spectroscopy. The modified electrodes were characterized using cyclic voltammetry and electrochemical Impedance spectroscopy.

The introduction of metal ion in the center of the porphyrin improved electrocatalysis. The presence of push-pull substituents in the porphyrin lowered the oxidation potential and improved the catalysis. The presence of GQDs improved catalysis in both symmetric and asymmetric porphyrin compared to individual components. Cobalt porphyrins showed better activity than manganese porphyrin.

Table of contents

Acknowledgements i

Abstract ii

Table of contents iii

List of abbreviations vi

List of symbols vii

Preamble viii

Chapter 1

1. Introduction 1

1.1 Porphyrins 1

1.1.1 Background 1

1.1.2 Synthesis of Porphyrin 2

1.1.3 Absorption spectra of porphyrin 3

1.1.4 Electrocatalysis 4

1.1.5 Metallopoprhyrin in electrocatalysis 6

1.1.6 Porphyrins applied in this work 9

1.2 Graphene quantum dots (GQDs) 11

1.2.1 Overview 11

1.2.2 Synthesis 12

1.2.2.1 Top-down 12

1.2.2.2 Bottom-up 13

1.2.3 Application of GQDs 14

1.2.4 Porphyrin-GQDs in electrocatalysis 15

1.3 Analyte 16

1.4 Aims and objectives 16

Chapter 2

2. Experimental 17

2.1 Materials 17

2.2 Equipment 17

2.3 Synthesis of porphyrins (manganese 5, 10, 15-tris(aminophenyl) -20-(4-carboxyphenyl) porphyrin chloride [2-Mn], and cobalt 5, 10, 15-tris(aminophenyl)-20-(4-carboxyphenyl) porphyrin [2-Co]) 18

2.4 Formation of conjugates 19

2.5 Electrode Modification 20

Publications 21

Chapter 3

3. Results and Discussion 22

3.1 Formation of MPs and GQDs composites, mass spec and FT-IR 22

3.2 UV-Vis spectroscopy 25

3.3 Dynamic light scattering (DLS) and transmission electron microscopy (TEM) 28

3.4 X-ray diffraction (XRD) patterns and energy dispersive spectroscopy (EDS) 31

3.5 X-ray photoelectron spectroscopy (XPS) studies 32

3.6 Conclusions 34

Chapter 4

4. Characterization of Modified Electrode 35

4.1 Characterization in ferricyanide solution 35

4.1.1 Cyclic voltammetry (CV) 35

4.1.2 Electrochemical impedance spectroscopy (EIS) 38

4.2 Characterization in 0.1M NaOH buffer 40

4.3 Conclusions 43

Chapter 5

5. Electrocatalytic detection of Hydrazine 44

5.1 Cyclic voltammetry 44

5.2 Kinetic studies of Hydrazine detection 47

5.3 Chronoamperometric studies 51

5.4 Interference studies 55

5.5 Summary 57

Chapter 6

6. Conclusions 58

6.1 Future aspects 59

References 60

Appendix 70

List of abbreviations

CV	cyclic voltammetry
DCM	dichloromethane
DMF	N, N-dimethylformamide
DLS	dynamic light scattering
EDS	energy dispersive x-ray spectroscopy
EDC	1-Ethy-3-(3-dimethylaminopropyl)-carbodiimide
EIS	electrochemical Impedance spectroscopy
FT-IR	Fourier transform - infrared
GCE	glassy carbon electrode
GQDs	graphene quantum dots
HOMO	highest occupied molecular orbital
LED	Light-emitting diode
LoD	limit of detection
LUMO	lowest unoccupied molecular orbital
MeOH	methanol
NHS	N-hydroxysuccinimide
P	porphyrin
Redox	reduction/oxidation
TEM	transmission electron microscopy
UV-Vis	ultraviolet-visible
XRD	x-ray diffraction
XPS	x-ray photoelectron microscopy

List of symbols

A	absorbance/surface area
K	catalytic rate constant
C	concentration
I	current
ΔG°	change in Gibbs free energy
ε	molar extinction coefficient
α	non-peripheral position
Ip	peak current
Ep	peak potential
ΔEp	peak to peak potential separation
β	peripheral position
v	scan rate
Γ	surface coverage
λ	wavelength
T	temperature

Preamble

In this thesis, cobalt and manganese porphyrin and graphene quantum dots (GQDs) are synthesised. The synthesized metalloporphyrins are incorporated into GQDs via covalent and π-π stacking to form metalloporphyrin-GQDs composites. The success of the synthesis if confirmed by various spectroscopic and electrochemical characterization. The thesis also covers the electrocatalytic activity of the synthesized metalloporphyrin-GQDs composites for the electro-oxidation of hydrazine. The effect of metal ion is investigated, and the types of substituents at the meso position of the porphyrin is explored. The effect of attachment of porphyrin to graphene quantum dots via π-π stacking in comparison to covalent linking is also explored.

Chapter 1:

Introduction

This chapter provides a brief history of porphyrin, graphene quantum dots and the composites.

1. Introduction

1.1 Porphyrins

1.1.1 Background

Porphyrins are aromatic macrocyclic molecules containing 22 π-electrons, but only 18 of these are required for its conjugated aromatic network. The porphyrin structure is made of four pyrrole units and four bridging carbon atoms in a planar conformation [1,2] Fig. 1.1. The structure of porphyrin is found in nature in various types of chlorophylls and hemes [1,3,4]. The convention of incident light into chemical energy by chlorophyll during photosynthesis has inspired many scientists to study porphyrin derivatives and their metalated forms [5,6]. Porphyrin research has a long history, covering a broad variety of disciplines of natural sciences, including photosynthesis, photodynamic therapeutic agents, chemosensors, conductive organic materials, light emitting materials, near-infrared dyes, nonlinear optical materials, electrocatalysis and more [1].

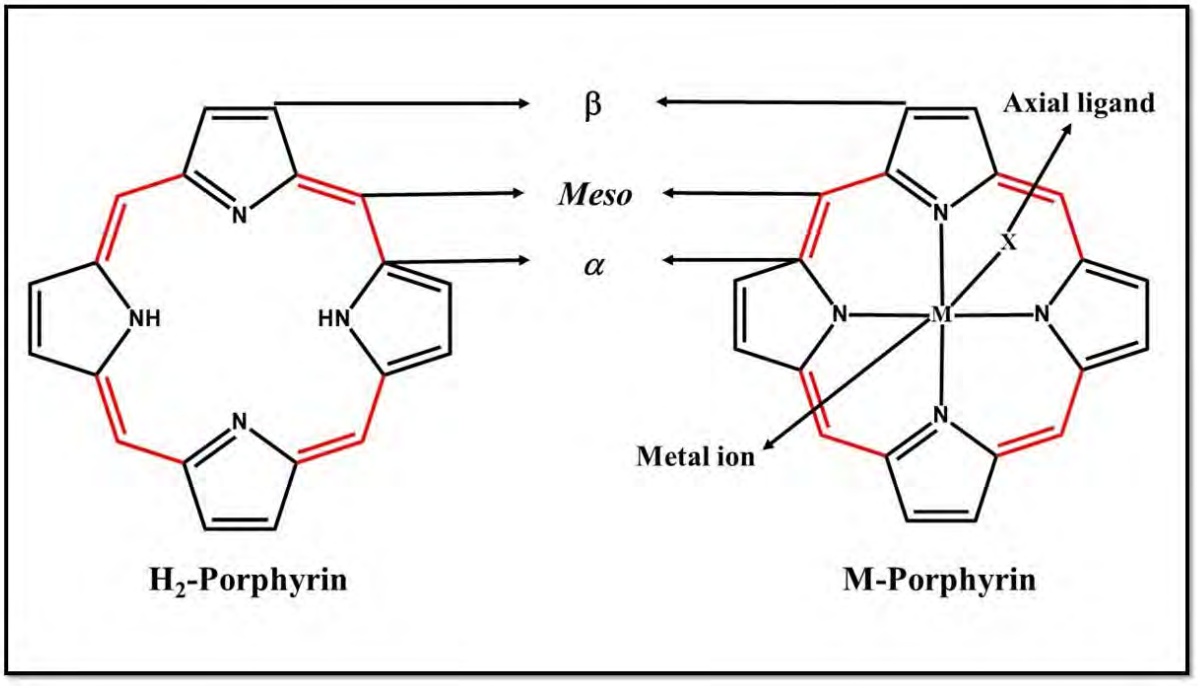

Fig. 1.1. Basic porphyrin ring structure. Pyrrolic rings are represented in black while methine bridges are presented in red.

A porphyrin molecule can undergo addition and substitution reaction without losing its aromaticity [1,2]. The porphyrin ring consists of meso, β, and α substitution positions. The meso position is the most electronically active and the preferential site for substitutions. The porphyrin structure can coordinate metals to form metalloporphyrin [7].

1.1.2 Synthesis of Porphyrin

There are various methods of synthesizing porphyrins including, Rothemund and Menotti [8], Lindsey [9], Microwave-assisted [10], and Adler and Longo [11] Scheme 1.1. The synthesis of all porphyrins in this work was carried out using the Adler and Longo method with pyrrole, aldehyde of choice in propionic acid [11].

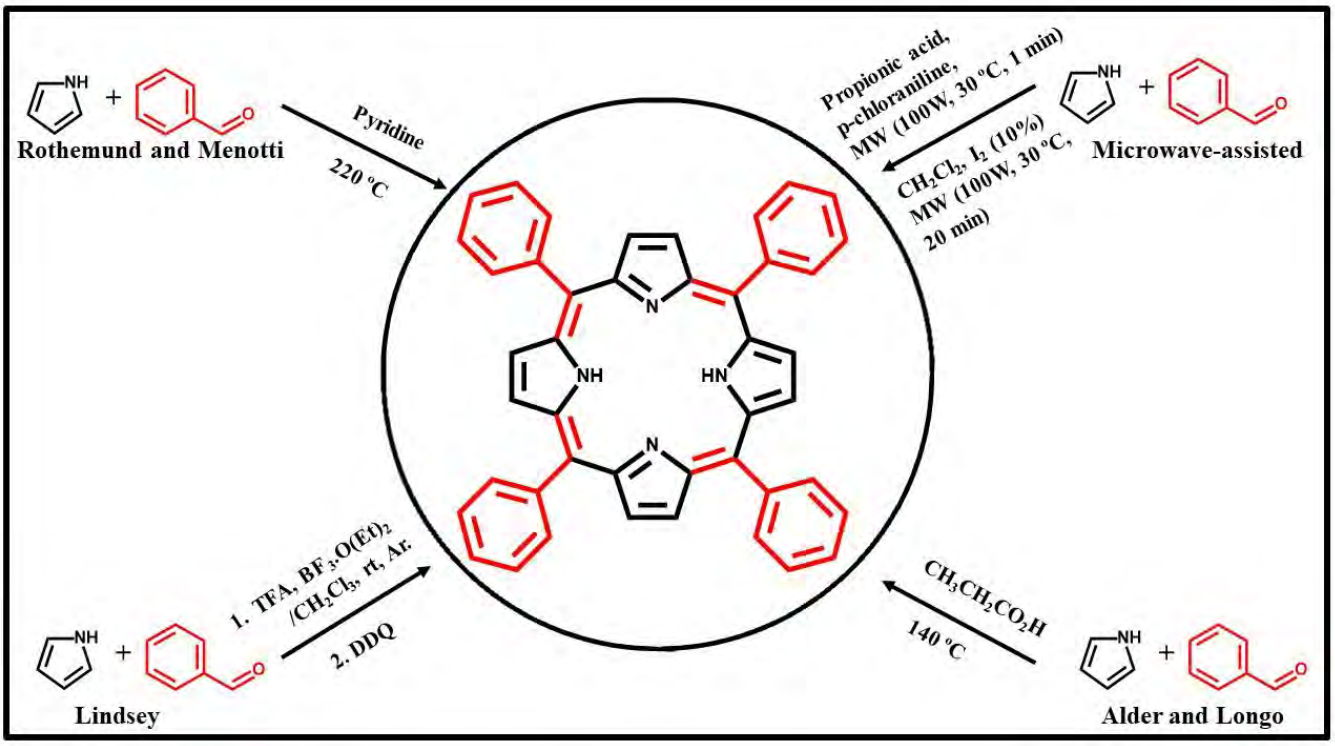

Scheme 1.1. Schematic representation of a free base porphyrin synthesis using different methods under different reaction conditions.

Symmetric porphyrins can either be meso or β substituted depending on the method of substitution [12]. Tetra meso porphyrins are prepared by condensation of pyrrole with aldehyde in propionic acid. On the other hand, asymmetric porphyrins are normally synthesized by condensation of pyrrole and the appropriately substituted benzaldehydes

(A+B) in a 3:1 ratio, Scheme 1.2. This result in the formation of the desired mono substituted porphyrin with mixture of tetraphenyl porphyrin, and tri-, di-, and tetra substituted compounds [13], which have to be separated by chromatography.

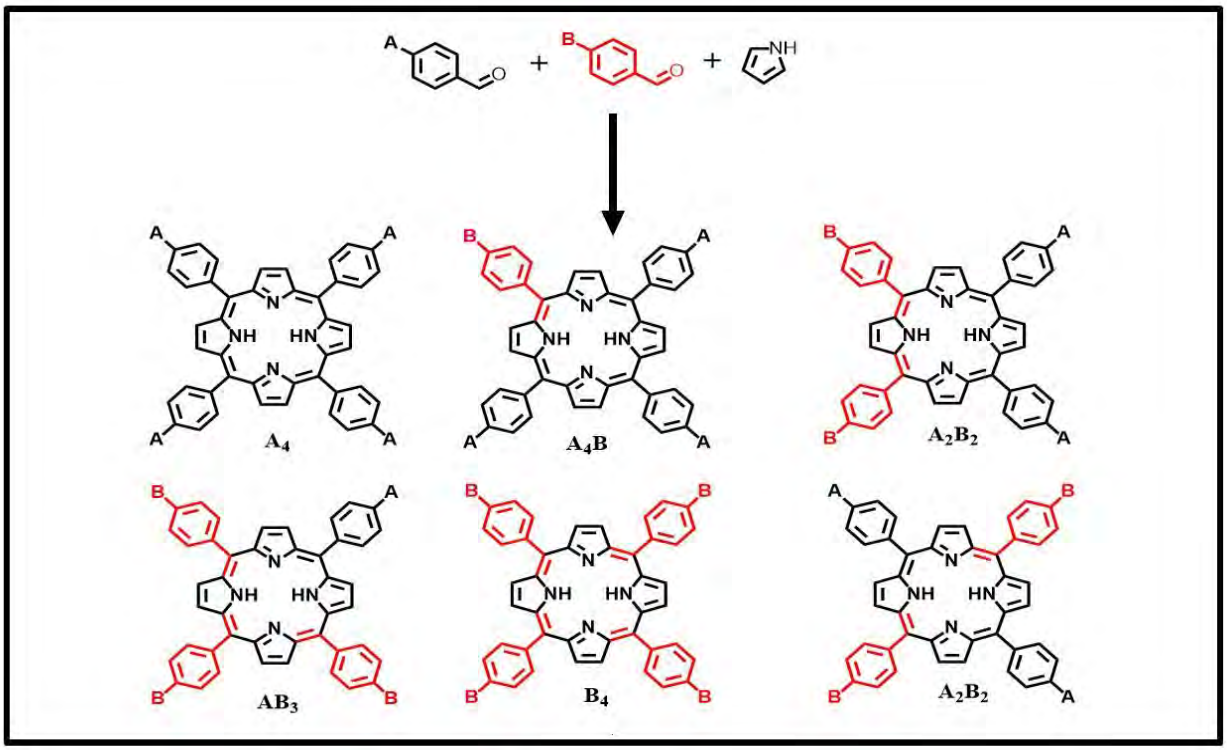

Scheme 1.2. Schematic representation of possible symmetric and asymmetric porphyrin products that can form from a general porphyrin synthesis using a ratio of 3:1.

1.1.3 Absorption spectra of porphyrin

The absorption spectra of porphyrins are explained by Gouterman's theory which states that the absorption bands of porphyrins are as a result of transitions from the two highest occupied molecular orbitals (HOMOs); that is a_{1u} and a_{2u}, to the lowest unoccupied molecular orbitals (LUMOs); e_g, and the relative energies of these transitions are affected by the nature of the metal center and substituents on the porphyrin ring [11,14], Fig. 1.2. (insert).

Porphyrins absorb strongly in the visible region near 400 nm (Soret band), and weaker absorption bands between 500-650 nm known as Q bands [15]. Metalation of the porphyrin collapses the four Q bands of free base porphyrin into two, Fig. 1.2 [16].

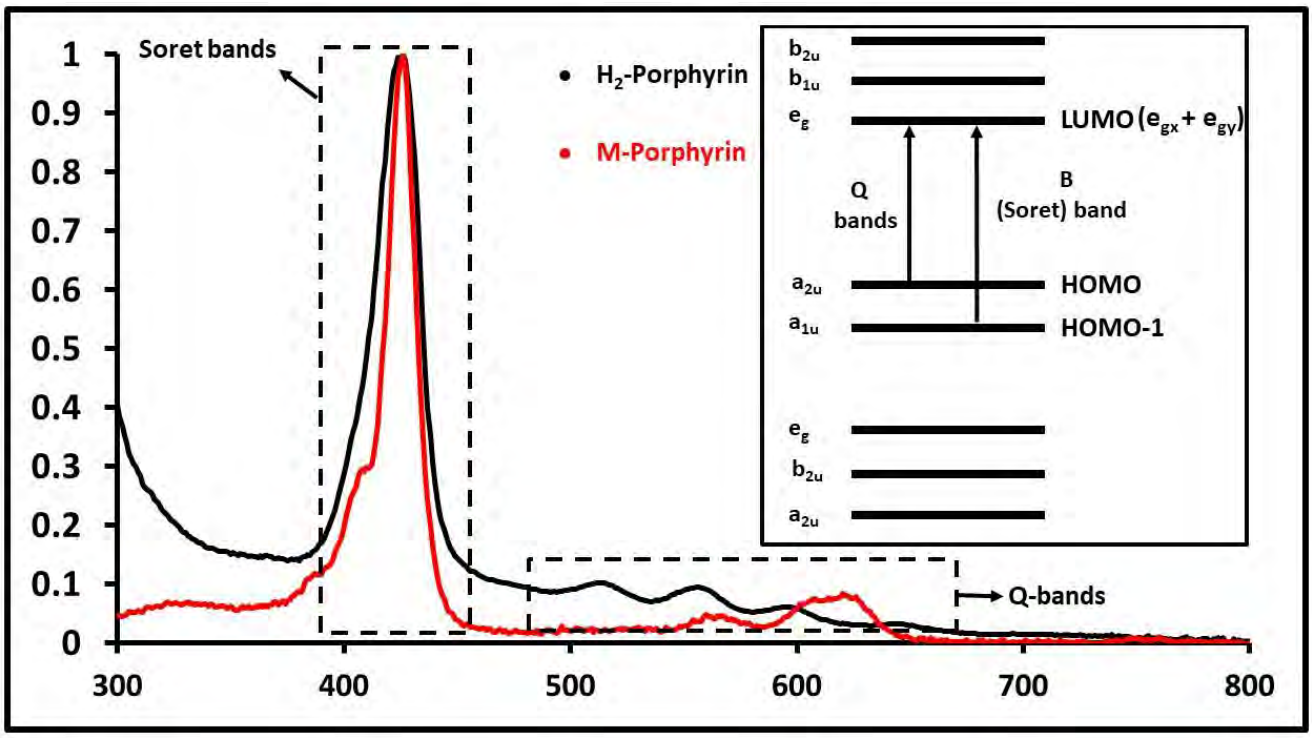

Fig. 1.2. The UV-visible absorption spectra of a unmetalated porphyrin (H2-porphyrin) and metalated porphyrin (M-Porphyrin); showing the change in the position of Soret band and the collapse of Q bands. Origin of the transition shown as insert ($a_{1u} \rightarrow e_g$).

1.1.4 Electrocatalysis

Electrocatalysts improves the rate of an electrochemical reaction occurring on an electrode surface. They transform non-selective, unmodified surfaces into more sensitive and selective sensors. In simple terms electrocatalysis is a combination of electrochemistry and catalysts [17,18]. Electrochemical methods show high sensitivity and selectivity, surpassing atomic absorption spectroscopy, atomic emission spectroscopy, inductively coupled plasma mass spectroscopy, and chromatography [19].

The presence of electrode modifier changes the electrochemical behavior of the electrode [20]. The role of electrocatalyst is to increase the rate of the electrode reaction, which result in an increase in current, Fig. 1.3 and lowering of potential.

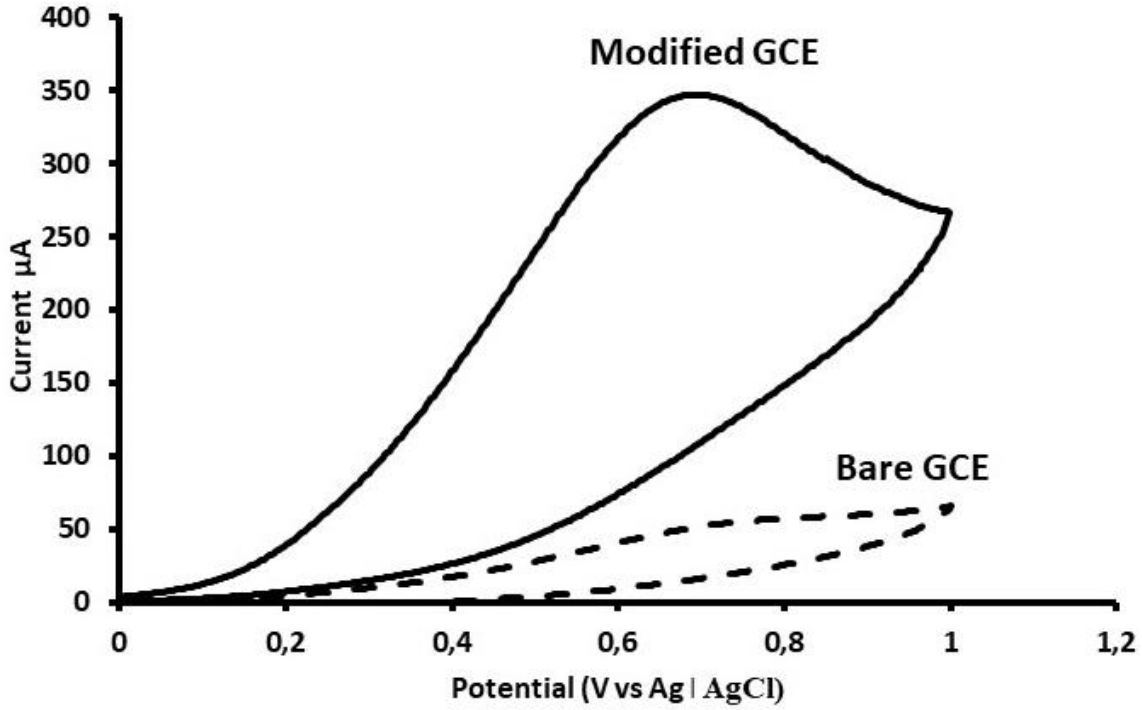

Fig. 1.3. Cyclic voltammograms of a bare GCE and a modified GCE in 0.1 M NaOH in 1 mM Hydrazine. [Unpublished work].

Electrocatalysis, as with chemical catalysis, can either be homogenous or heterogeneous in character. In the case of homogenous electrocatalysis, both the catalysts and the substrate are in the same phase in solution. In heterogeneous electrocatalysis, the catalyst is immobilized on the electrode surface. Porphyrins are used as heterogeneous catalysts in this work, due to their ability to quickly lose their reactivity when removed from the electrode.

The modification of electrodes can be achieved in various ways depending on the type of catalyst and electrode. Methods of modification that are commonly employed are drop-dry method, spin-coating, electrodeposition, modified carbon paste electrode, self-assembled monolayers etc. [21]. The least complicated method is drop-dry method and is the selected method of modification for this work. In this method a catalyst is dissolved in an appropriate

solvent and a few drops of the solution are applied to the electrode surface and the solvent is allowed to dry [20] Fig. 1.4. When the solution is dried, the modified electrode is then introduced in an electrochemical cell containing the analyte of interest and electrochemical studies are performed. Porphyrins and graphene quantum dots are applied in this thesis for their electrocatalytic ability [22].

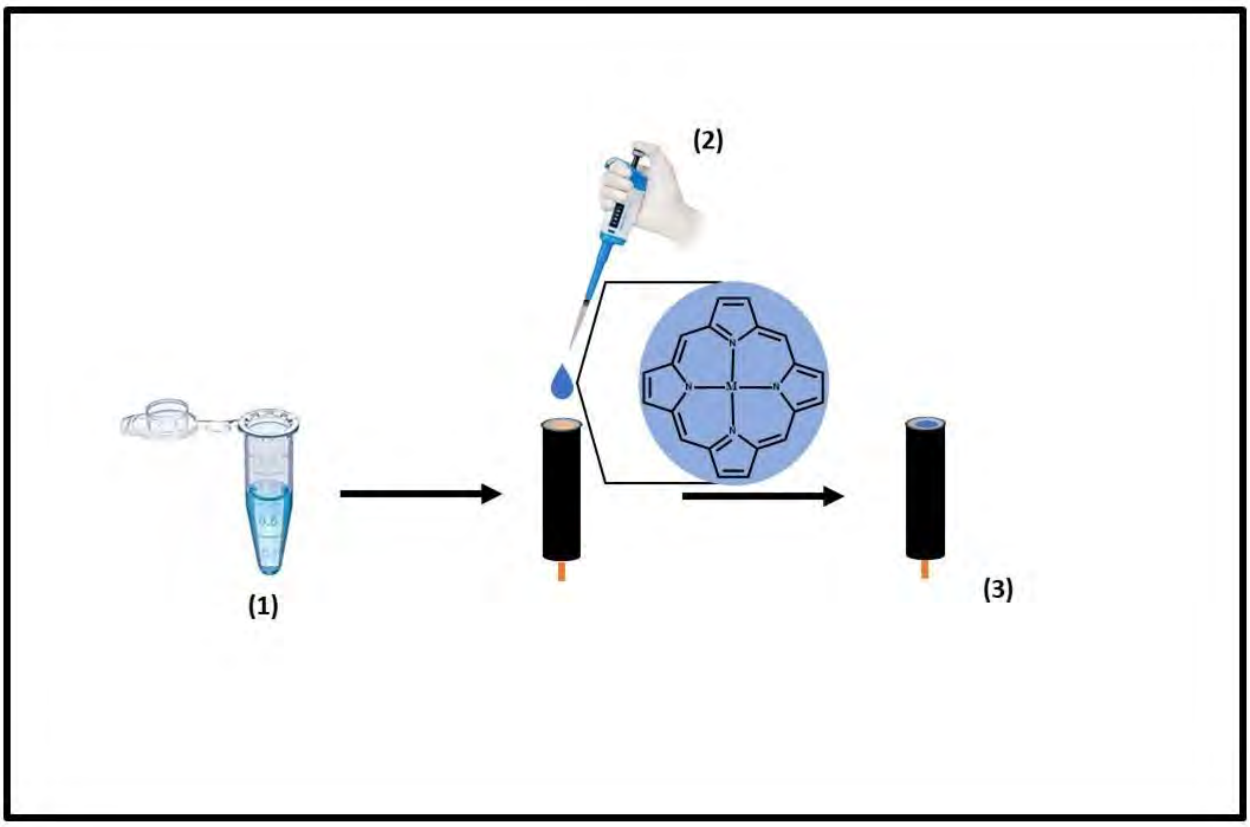

Fig. 1.4. General procedure of drop-dry method on a bare GCE. (1) Solution of porphyrin, (2) drop casting of porphyrin solution, (3) Drying in an inert environment.

1.1.5 Metallopoprhyrin in electrocatalysis

The ability to modify porphyrins with various types of substituents and with almost all the transition metal ions has made porphyrins vital electrocatalysts applied in electrochemistry [5]. These modifications alter electronic properties of the porphyrin such as redox processes, light absorption properties, energy and electron transfer [5]. The rich redox chemistry of metalloporphyrins make them ideal for electrocatalysis [22]. The attachment of redox active metalloporphyrins to electrodes simplifies the electrochemical study and facilitates

electrocatalysis [23]. Table 1.1 [22,24-32] shows that there are no asymmetric porphyrins used for the detection of hydrazine. Asymmetry improves electrocatalytic activity [33] hence asymmetric porphyrins are employed in this work.

Table 1.1. The porphyrins which have been used for electrocatalytic detection of hydrazine.

Porphyrin	
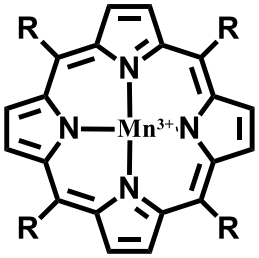 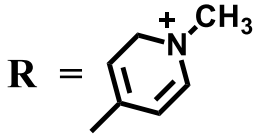	[22]
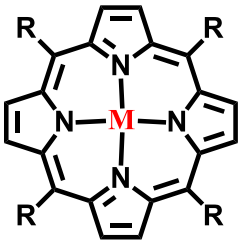 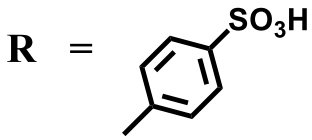	M = Ni [24] M = Mn [25] M = Co [26]
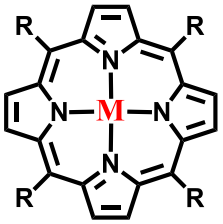 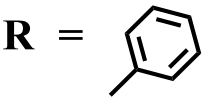	M = Cu [27] M = Co [28]

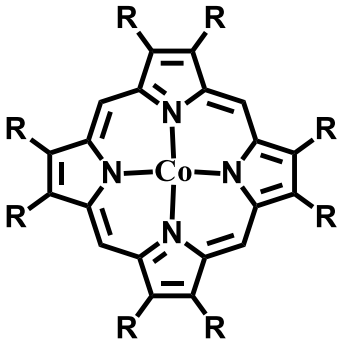

R =

[29]

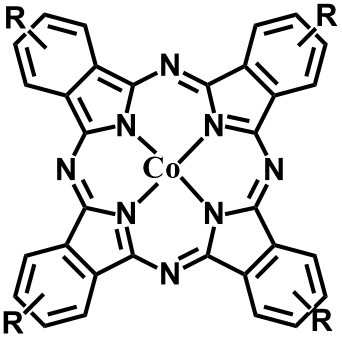

R =

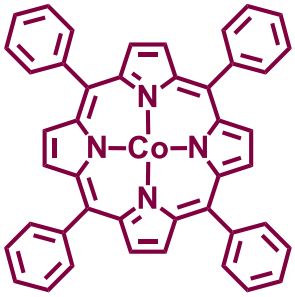

[30]

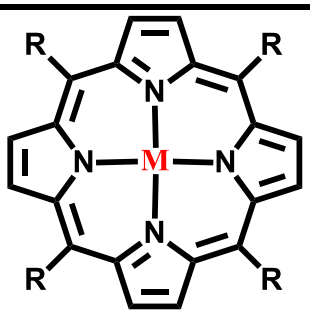

R =

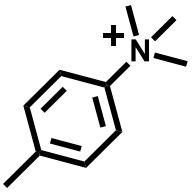

M = H2 [31]

M = Co [32]

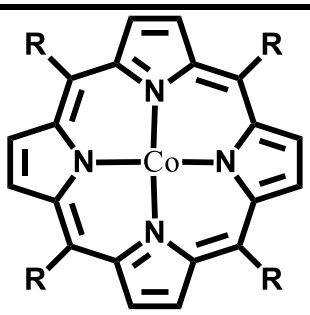

R = 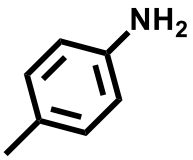

[32]

R = 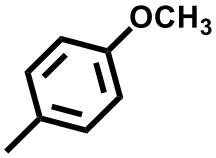

[26]

R = 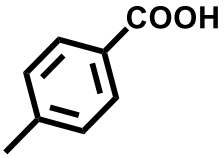

[26]

1.1.6 Porphyrins applied in this work

Table 1.2 provides information about the porphyrins used in this work. All are new except **1**-H2 [34] and **1**-Mn [35]. In this study, porphyrins and graphene quantum dots (GQDs) are synthesized and their effect in electro-oxidation of hydrazine is explored. The effect of metal center is studied by comparing the activity of complex **1**-H_2 with complex **1**-Mn and by comparing complex **2**-Co to **2**-Mn. The effect of symmetry is also studied through comparison of complex **2**-Mn and **1**-Mn. Lastly, the nature of attachment of porphyrin to GQDs and the effect it has on the electro-oxidation of hydrazine is investigated. This is achieved by comparing complex **1**-Mn--GQDs (π-stacking) to **1**-Mn@GQDs (covalent linking).

Table 1.2. Porphyrins employed in this work. All used for hydrazine detection.

Structure	Complex name
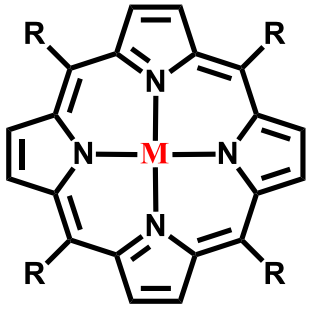 **M = Mn** **M = H_2** **R =** 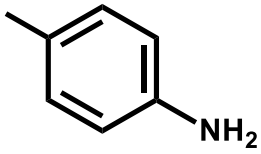	**Tetrakis 4-aminophenyl porphyrin (1-H_2) [34]** **Manganese Tetrakis 4-aminophenyl porphyrin (1-Mn) [35]**
1-Mn--GQDs	**Tetrakis 4-aminophenyl porphyrin-GQDs (1-Mn--GQDs) [New]**
1-Mn@GQDs	**Tetrakis 4-aminophenyl porphyrin@GQDs (1-Mn@GQDs) [New]**
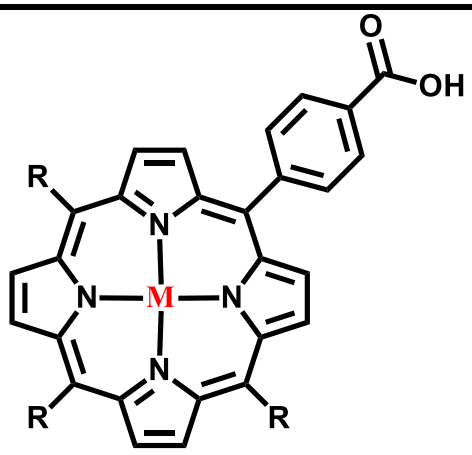	**Cobalt 5, 10, 15-tris(aminophenyl)-20-(4-carboxyphenyl) porphyrins (2-Co) [New]** **Manganese 5, 10, 15-tris(aminophenyl)-20-(4-carboxyphenyl) porphyrins (2-Mn) [New]** **2-H_2 [Not known]**

R = 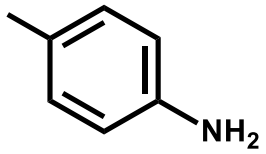 M = Co M = Mn	
2-Mn--GQDs	Manganese 5, 10, 15-tris(aminophenyl)-20-(4-carboxyphenyl) porphyrins-GQDs (2-Mn--GQDs) [New]
2-Co--GQDs	Cobalt 5, 10, 15-tris(aminophenyl)-20-(4-carboxyphenyl) porphyrins-GQDs (2-Co--GQDs) [New]

1.2 Graphene quantum dots (GQDs)

1.2.1 Overview

Graphene is a two dimensional (2D) planar structure with carbon atoms arranged in a honeycomb lattice with sp^2 hybridization. Graphene attracted scientists attention as early as 1947 [36]. Because of its excellent electronic properties, graphene is now one of the most studied materials. Graphene quantum dots (GQDs) are zero-dimensional carbon-based nanoparticles consisting of thin graphene sheets that are generally functionalized with (carboxylic, hydroxyl, carbonyl, epoxide) on their edge. GQDs normally have dimension in the size range below 20 nm diameter [36,37]. The functional groups and the method of preparation of GQDs determines their spectroscopic properties. The interesting properties of GQDs including low toxicity, high solubility, the presence of functional groups at the edges which allowed the application of GQDs in for example solar cells, photodetectors, bioimagings, fluorescent agents, light-emitting diodes (LEDs), batteries, sensors, drug carriers, photo-/electro-catalytic, etc [38].

1.2.2 Synthesis

The two main synthetic approaches of preparing GQDs are top-down and bottom-up methods.

1.2.2.1 Top-down

Top-down approach involves a controlled reduction of large macroscopic materials to obtain a nanosized material with unique features which are better than those of the starting material [36], Scheme 1.3. The ordinary materials used in the synthesis of GQDs using the top-down approach includes graphite, coal, graphene, carbon fibres, and graphene oxide [38]. Various techniques such as solvothermal and hydrothermal methods, liquid exfoliation, electrochemical, oxidation, microwave-assisted exfoliation and ultrasonic etc., have been employed for top-down synthesis of GQDs [37,39].

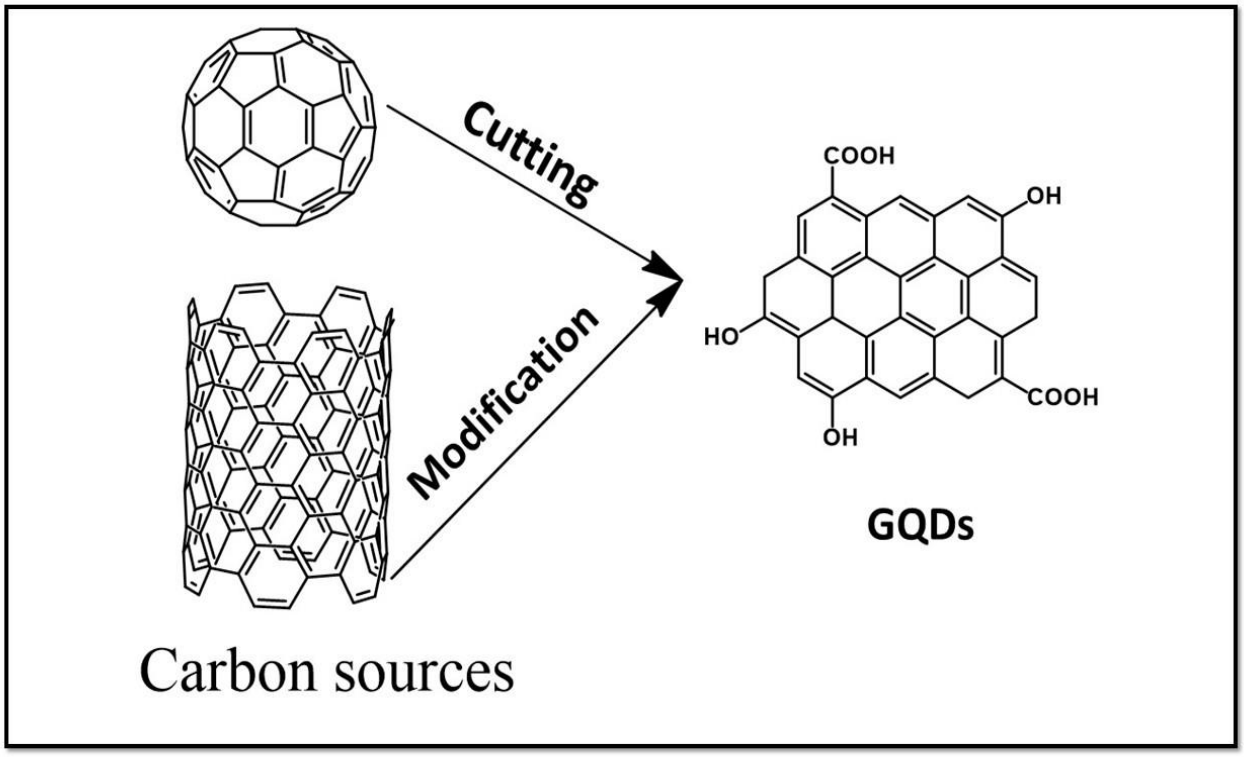

Scheme 1.3. Schematic representation of GQDs synthesized using a top down approach.

The hydrothermal and solvothermal methods vary in the sense that the former uses water as a solvent while the latter uses organic solvents. Both methods make use of high pressure and high temperatures to cut carbon materials into GQDs. In addition, the carbon material requires treatment with strong acids before the actual reaction can take place [37-41]. Ultrasound is also reported to produce GQDs from graphene sheets and also requires the oxidation of graphene sheets with concentrated sulfuric acid or nitric acid [39]. Microwave assisted synthesis also breaks down large materials into nanomaterials using a shorter reaction time. This method is reported to be one of the mostly used methods as it is faster and improves the production yield of GQDs [42]. Another mostly used method is oxidative cleaving also referred to as oxidative cutting, this approach makes use of oxidizers such as sulfuric acid/nitric acid to cut carbon nanotubes into smaller pieces [43]. Electrochemical oxidation is also another method that produces GQDs where carbon material work as a working electrode and is cleaved into GQDs under high voltage [43,44].

1.2.2.2 Bottom-up

The bottom-up approach uses small molecules such as citric acid to build up GQDs, Scheme 1.4. As much as the top-down approach produces GQDs in large scale and requires less purification, the bottom-up approach is reported to be better than the top-down approach as it allows a more controllable synthesis, is cheaper, shows less defects and provides good carbonation with a reasonable size range [36,45,46]. Citric acid is mostly used in the synthesis as a precursor to hydrothermally produced GQDs. Bottom-up route also has a number of different sub techniques, this includes microwave assisted hydrothermal treatment and carbonization (direct pyrolysis) [36,37,43,47]. Bottom-up method was used in synthesizing the GQDs used in this thesis.

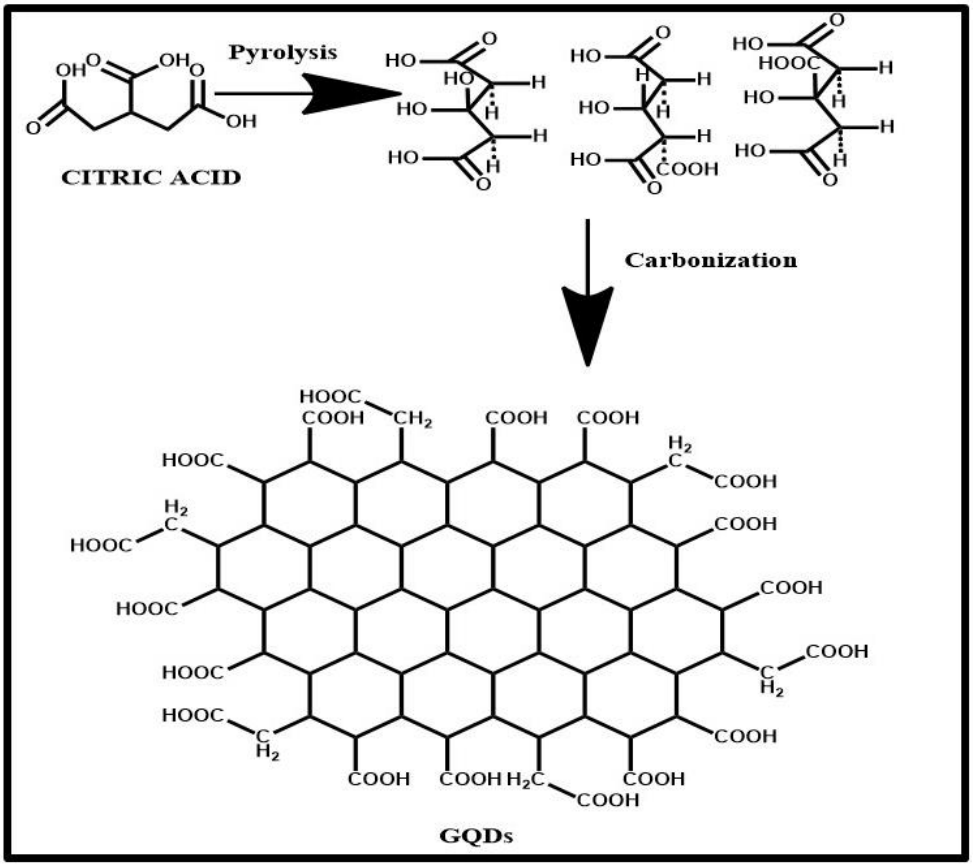

Scheme 1.4. Schematic diagram of GQDs obtained from citric acid using the bottom up methods [37].

1.2.3 Application of GQDs

It is believed that GQDs may become a popular material for advanced technology. Researchers have been exploring the functionalization of GQDs with various molecules for application in different fields. GQDs have already been exploited in a number of applications, such as biological imaging, sensors, drug delivery, photodetector, light emitting diodes (LEDs), and batteries etc. [38]. Recent interest has been in the development and application of GQDs in electrochemical sensors and biosensors [38,48]. Properties such as electrocatalytic activity and high-speed electron transport, have opened a channel for the application of GQDs in electrochemical sensing [49]. GQDs in sensing are mostly used to modify electrodes to improve electrochemical sensing [50]. In this thesis, the focus is on the GQDs ability to improve the electrocatalysis of porphyrins.

1.2.4 Porphyrin-GQDs in electrocatalysis

GQDs and porphyrin have both been applied for catalysis separately and combined. Several studies have reported the application of porphyrin-GQDs combination for sensing of various analytes Table 1.3 [51-57]. This work reports for the first time on the use of: (1) GQDs-porphyrin composite and (2) asymmetric porphyrin, for hydrazine detection. Table 1.3. shows that no porphyrin-GQDs for hydrazine detection. Only π-stacking porphyrin-GQDs applied for sensing of other analytes and only symmetrical porphyrins employed, hence explored in this work.

Table 1.3. Porphyrin GQDs combination for electrocatalysis.

Conjugate	Application	Interaction	Reference
NGQs-TMPyP	Cadmium (II) sensing	π-stacking	[51]
Cop-BNF/SNGQDs@AuNPs/Transtuzumab	HER2 detection	π-stacking	[52]
GQDs-H_2TprP, GQDs-GaClTPrP, GQDs-ZnTPrP	Photophysical studies	π-stacking	[53]
M-GQDs-TAPP	Biothiols sensing	π-stacking	[54]
GQDs-TPP, GQDs-TNaP	Fluorescence studies	π-stacking	[55]
GQD-PEG-P	miRNA detection	π-stacking	[56]
CoTSPP@N, P: GQDs/G	Photocatalysis	π-stacking	[57]

NGQDs – Nitrogen-doped graphene quantum dots; TMPyP – Tetrakis(1-methyl-4-pyridinio) porphyrin; Cop-BNF – Cobalt porphyrin binuclear framework; SNGQDs – Sulfur/nitrogen-doped graphene quantum dots; AuNPs – Gold nanoparticles; HER2 – Human epidermal growth factor receptor 2; H_2TPrP – Meso-tetra(pyren-1-yl) porphyrin; M-GQDs-TAPP – Maleimide functionalized graphene quantum dots-Tetrakis(4-aminophenyl) porphyrin; TPP – Tetraphenyl porphyrin; TNaP – Tetranaphthyl porphyrin; GQD-PEG-P – Graphene quantum dots-polyethylene glycol-porphyrin; CoTSPP@N, P: GQDs/G – Cobalt porphyrin-supported nitrogen-phosphorus co-doped graphene quantum dots/graphene.

1.3 Analyte

Hydrazine is widely used as a starting material in the production of insecticides, herbicides, pesticides and is also used in pharmaceutical industries. Hydrazine is one of the most commonly analyzed compounds in industrial and environmental samples owing to toxicity [58].

The environmental impacts caused by hydrazine contamination and accumulation are significant concerns in terms of human health [58]. The maximum recommended levels of hydrazine in trade effluents is 1 ppm (0.000031 mol/L) [59,58]. However, workers who are in close contact with hydrazine during routine maintenance tasks can be exposed to levels way above the National Institute for Occupational Safety and Health reactive exposure limits [59], hence the need to detect hydrazine.

1.4 Aims and objectives

In this work we modify the surface of a glassy carbon electrode with graphene quantum dots and metalloporphyrin to improve the sensing ability of the electrode and to enhance the electro-oxidation of hydrazine.

The objectives of the work are to

- Synthesize symmetric and asymmetric metalporphyrins with manganese and cobalt as metal ions, perform a spectroscopic and electrochemical characterization and apply them for electro-oxidation of hydrazine.
- Synthesize GQDs
- Covalent link of GQDs to metalloporphyrin
- Non-covalent link (π-π stacking) of GQDs to metalloporphyrin
- Characterize metalloporphyrin-GQDs nanocomposite
- Modify the electrodes with the synthesized compounds
- Apply the modified electrodes for electro-oxidation of hydrazine.

Chapter 2:

Materials and Experimental

This chapter gives a list of material and equipment used and outlay the synthetic procedures applied.

2. Experimental

2.1 Materials

N,N dimethyl formamide (DMF) and dichloromethane (DCM) were purchased from Merck. Aniline was purchased from BDH laboratory chemical. Ammonia, methanol, manganese (ll) chloride ($MnCl_2$), cobalt (ll) chloride, tin (II) chloride, *N*-hydroxysuccinamide (NHS), 1-ethyl-3-(3-dimmethylaminopropyl) carbodiimide (EDC), hydrazine monohydrate, sodium hydroxide, 4-nitrobenzaldehyde, and 4-formylbenzoic acid were all obtained from Sigma Aldrich. All chemicals were used without further purification. Type II water from ELGA Lab Water was used for the aqueous solutions. The graphene quantum dots (GQDs) [60], tetra 4-aminophenyl porphyrin (complex **1**-H_2) [34], manganese tetra 4-aminophenyl porphyrin (complex **1**-Mn) [35] and 5, 10, 15-tris(aminophenyl)-20-(4-carboxyphenyl) porphyrin (**2**-H_2) [61] were synthesized as reported in literature.

2.2 Equipment

1. UV-Vis absorption spectra were obtained from a Shimadzu UV-2250 spectrophotometer.
2. Infrared (IR) spectra were recorded with a Bruker Alpha IR (100 FT-IR) spectrophotometer.
3. The mass spectral data was acquired from a Bruker AutoFLEXIII smart-beam TOF/TOF mass spectrometer using cyano-4-hydrocinnamicacid as the matrix.
4. The elemental analysis was conducted using a Vario-Elementar Microcube ELIII.
5. Energy dispersive X-ray spectroscopy (EDS) was done on an INCA PENTA FET coupled to the VAGA TESCAM using 20 kV accelerating voltage.
6. X-ray diffraction (XRD) spectra were performed on a Bruker D8 Discover diffractometer, equipped with a LynxEye detector, under Cu-Kα radiation (λ=1.5405 Å).
7. X-ray photoelectron spectroscopy (XPS) spectral analyses were conducted using an AXIS Ultra DLD (supplied by Kratos Analytical) using Al (monochromatic) anode equipped with a charge neutralize.

8. Dynamic light scattering (DLS) experiments were done on a Malvern Zetasizer nanoseries, Nano-ZS90.
9. Transmission electron spectroscopy (TEM) images were obtained from Zeiss Libra TEM 120 Model operated at 90 kV.
10. Cyclic voltammetric, square wave voltammetry, chronoamperometry, and electrochemical impedance spectroscopy (EIS) data were recorded using an Autolab Potentiostat PGSTAT30 equipped with Nova software version 2.1.

2.3 Synthesis of porphyrins (manganese 5, 10, 15-tris(aminophenyl)-20-(4-carboxyphenyl) porphyrin chloride [**2**-Mn**], and cobalt 5, 10, 15-tris(aminophenyl)-20-(4-carboxyphenyl) porphyrin [2**-Co**])**

5, 10, 15-tris(aminophenyl)-20-(4-carboxyphenyl) porphyrin (**2**-H_2) (15.0 mg, 0.0213 mmol) was dissolved in 20 mL DMF and heated at 120 ^oC, followed by the addition of $MnCl_2$ ((26.82 mg, 0.213 mmol) for **2**-Mn or $CoCl_2$ (36.88 mg, 0.284 mmol) **2**-Co). The mixtures were refluxed at 120 ^oC for 4 h. The resulting green solutions were cooled down, filtered, washed with water, and dried to give pure **2**-Mn and **2**-Co, Scheme 3.1. The mass spectra of **2**-Mn and **2**-Co are presented in Fig. A1 (appendix).

2-Mn: yield 35.55 mg (85%). FT-IR (UATR-TWOTM TM) max/cm $^{-1}$: 3326 (OH), 3214 (N-H), 1617 (C=O), 1460 (C=C), 1380 (C-N). MALDI-TOF-MS (m/z): cald = 792.16 $[M]^+$; found = 756.75 $[M\text{-}Cl]^+$. UV–Vis (DMF): λ max (nm) (log ε) 476 (5.83), 581 (3.08), 635 (3.23). Anal. Calculated ($C_{45}H_{31}ClMnN_7O_2$). $2H_2O$: C 65.26%, H 4.23%, N 11.88%. Found: C 65.05%, H 4.70%, N 12.03%.

2-Co: Yield: 41.50 mg (80%). FT-IR (UATR-TWOTM TM) max/cm $^{-1}$: 3310 (OH), 3220 (N-H), 1647 (C=O), 1633 (C=C), 1380 (C-N). MALDI-TOF-MS (m/z): cald = 760.71 [M]; found = 761.36 $[M]^+$. UV–Vis (DMF): λ max (nm) (log ε) 444 (4.68), 557 (2.57), 599 (2.59). Anal. Calculated ($C_{45}H_{31}CoN_7O_2$). $2H_2O$: C 67.84%, H 4.27%, N 12.31%. Found: C 68.52%, H 3.90%, N 12.03%.

2.4 Formation of conjugates

The interactions of the porphyrin with the GQDs were through π-stacking and covalent linkage, following the procedure reported in literature [62].

2.4.1 π-π interaction between porphyrin and GQDs

Briefly, each of the porphyrin derivatives (12 mg, 0.016 mmol for **1**-Mn, 19.0 mg, 0.023 mmol for **2**-Mn and 19.2 mg, 0.025 mmol for **2**-Co) were dissolved in DMF (3 mL), followed by addition of GQDs solution (10 mg/3mL) in water for **1**-Mn and (15 mg/3mL) in water for **2**-Mn and **2**-Co. The mixtures were sonicated for 4 h at room temperature. The mixtures were then left to stir for 24 h at room temperature. The products were precipitated with ethanol and washed several times with chloroform and water, and were dried to give complex **1**-Mn--GQDs, **2**-Mn--GQDs and complex **2**-Co--GQDs Scheme 3.2 (A).

2.4.2 Conjugation via amide bond

Covalently linked conjugate was prepared as follows: GQDs (7 mg) were dissolved in 6 mL water, then NHS (1.5 mg, 0.013 mmol), and EDC (1.5 mg, 0.0097 mmol) were added to the solution to activate the carboxylic acid groups of the GQDs. The mixture was left to stir for 24 h. **1**-Mn (7 mg, 0.0096 mmol) in DMF (3 mL) was added to the mixture which was left to stir for another 24 h. The product was precipitated with methanol. The precipitate was centrifuged and washed with water, methanol and chloroform. The conjugate is represented as complex **1**-Mn@GQDs Scheme 3.2 (B).

2.5 Electrode Modification

The glassy carbon electrode (GCE) was used as a working electrode, platinum wire as a counter electrode and silver|silver chloride (3 M KCl) as the reference electrode. The GCE was polished to a silver mirror on a Buehler felt pad using alumina (<10 μm) and washed with Millipore water and then sonicated in water for 5 min to remove impurities. The electrode was modified using the drop-dry method. The modification of electrodes was as follows: 5 μL (1 mg/mL) each of GQDs, **1**-H_2, **1**-Mn, **2**-Mn, **2**-Co, **1**-Mn--GQDs, **1**-Mn@GQDs, **2**-Mn--GQDs, and **2**-Co--GQDs, were dropped on the GCE and dried at 70 °C. The "--" sign represents the π-stacking while the "@" represent the covalently linked composites. All the modified electrodes were used to perform cyclic voltammetry (CV), electrochemical impedance spectroscopy (EIS) and chronoamperometry. Solutions for electrochemical experiments were deaerated by bubbling argon gas prior to the experiments and the electrochemical cell was kept under argon atmosphere throughout the experiments.

Publications

1. M. Jokazi, L.S. Mpeta, and T. Nyokong, Electrocatalytic activity of manganese tetra 4-aminophenyl porphyrin in the presence of graphene quantum dots. J. Electroanal. Chem, 2021, 901, 1-10.
2. M. Jokazi, L.S. Mpeta, and T. Nyokong, Electrocatalytic behavior of manganese and cobalt porphyrins attached to graphene quantum dots: Applied in the oxidation of hydrazine. [submitted, 13 May 2022].

Chapter 3:

Synthesis and characterization

This chapter discusses the results and characterization of the porphyrin, GQDs and their corresponding composites.

3. Results and Discussion

3.1 Formation of MPs and GQDs composites, mass spec and FT-IR

Scheme 3.1 shows the metalation of free base porphyrin **2**-H_2 to form **2**-Mn and **2**-Co. The complexes were characterized using UV-visible spectroscopy, mass spectrometry, elemental analysis, Fourier-transform infrared spectroscopy (FT-IR). Molecular ion peak for **2**-Co was observed at m/z = 761.36 in the mass spectrum. For **2**-Mn, was observed at m/z = 756.75 corresponding to the loss of the axial ligand, Fig. A1, Appendix. Elemental analysis confirms that porphyrins are isolated as hydrates [63]. Scheme 3.2 represents the attachment of porphyrin to GQDs via covalent and non-covalent attachment.

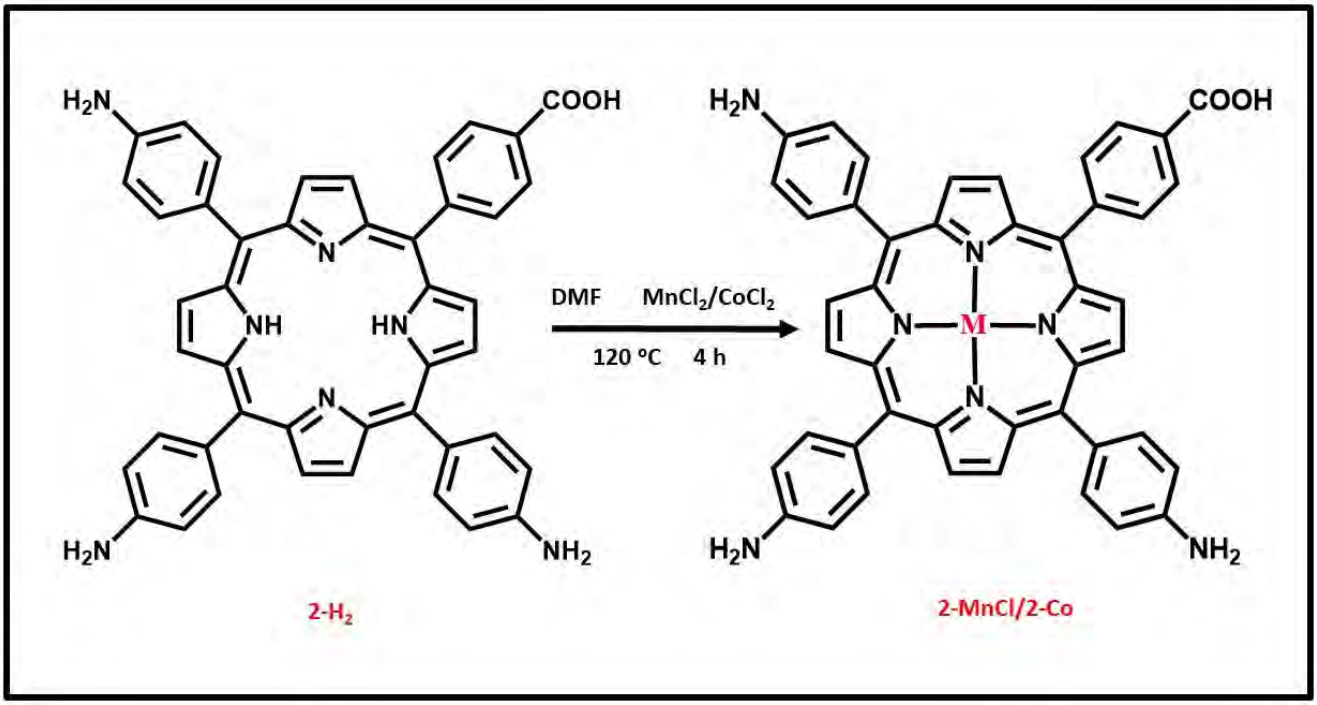

Scheme 3.1. Synthetic procedures of complex **2**-Mn, and **2**-Co.

A

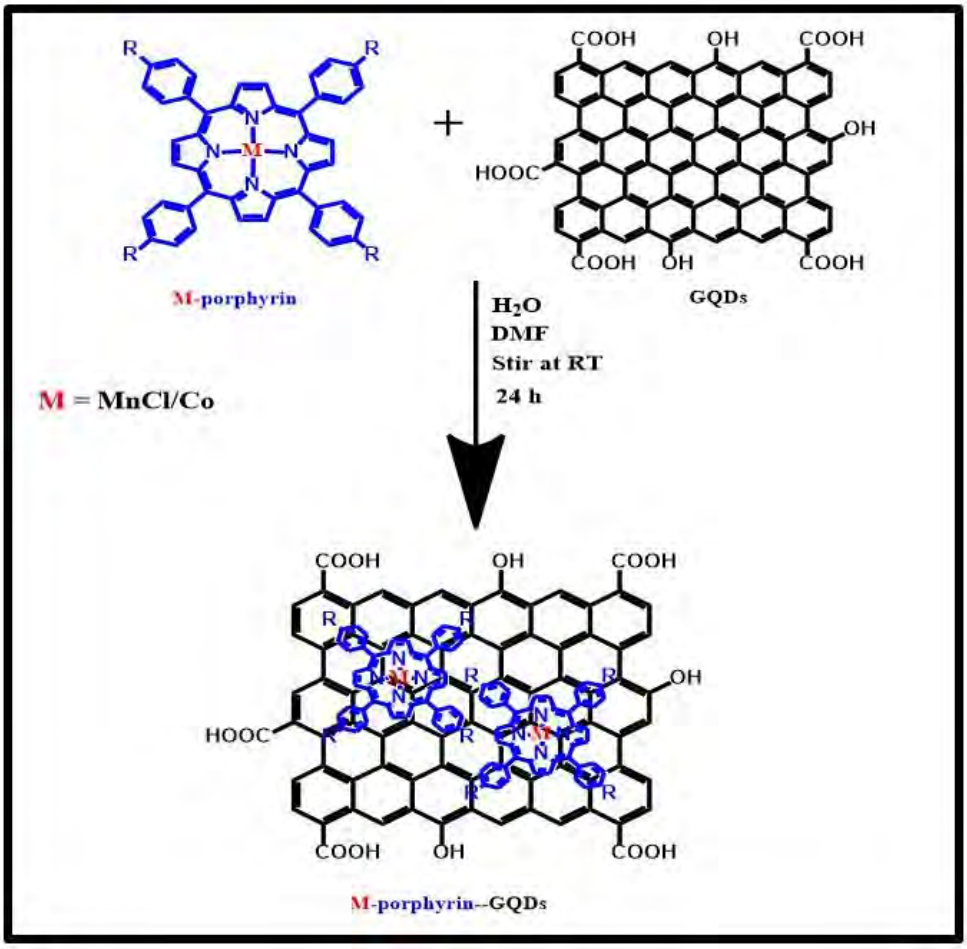
M-porphyrin
GQDs
H_2O
DMF
Stir at RT
24 h
M = MnCl/Co
M-porphyrin--GQDs

B

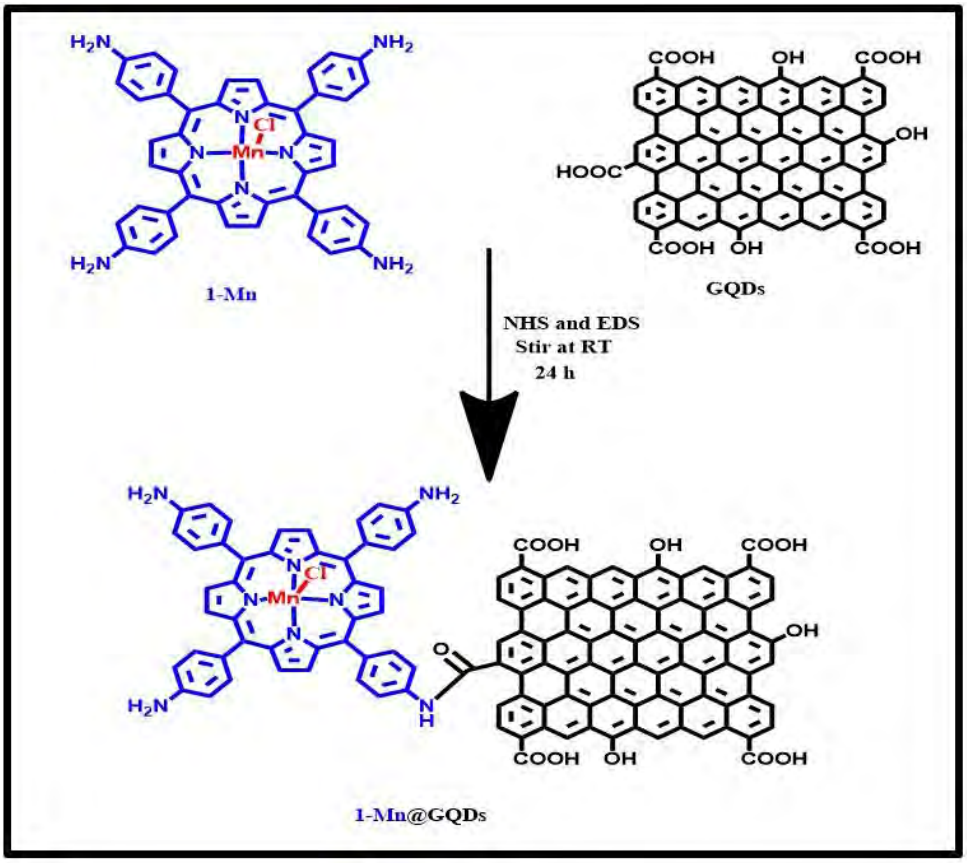

Scheme 3.2. The preparation of π-π stacked composites (A) and covalently linked composite (B).

FTIR spectra were also used to confirm the amide bond formation between **1**-Mn and GQDs Fig. 3.1. The FTIR spectrum of GQDs showed sharp peaks at 1674 cm^{-1} and 1397 cm^{-1} which correspond to the C=O stretching and C-O stretching of carboxylic acid [64]. The peak appearing at 3216 cm^{-1} belonged to OH and the C-H stretching appeared at 2918 cm^{-1} [64]. The peaks appearing at 3312 cm^{-1} and 3187 cm^{-1} on the FTIR spectrum of the **1**-Mn correspond to the symmetric and asymmetric vibration of NH_2. The stretching peak at 1590 cm^{-1} corresponds to the vibration of C-C and C-N. The peak appearing at 1558 cm^{-1} is the bending vibration of NH_2 group [65]. In the presence of GQDs the FTIR spectrum of **1**-Mn@GQDs showed a shift of the bending vibration of NH_2 from 1558 cm^{-1} to 1521 cm^{-1}. The shift and broadening of the vibration of C-C and C-N peak from 1590 cm^{-1} to 1731 cm^{-1} was observed and the appearance of a new peak at 1619 cm^{-1}, due to the amide bond. This shows that the linkage was successful for **1**-Mn@GQDs. It is also known that shifts in IR bands confirm structural changes [66].

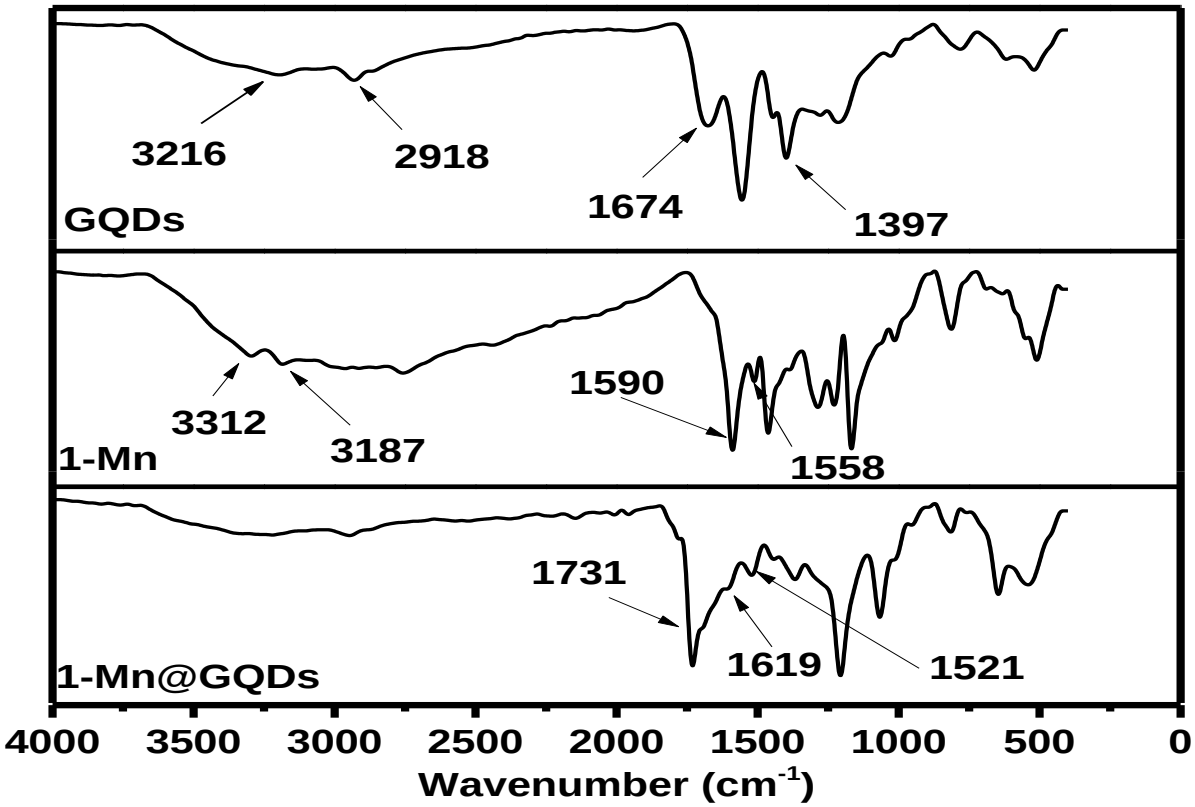

Fig. 3.1. The FTIR of GQDs, **1**-Mn, and **1**-Mn@GQDs.

3.2 UV-Vis spectroscopy

The absorption spectra of GQDs and porphyrins are shown in Fig. 3.2. All free base porphyrins have a similar visible spectrum with four absorption bands (Q bands) between 500-700 nm and the Soret band between 400-500 nm [15]. In Fig. 3.2. the free base porphyrin **1**-H_2 showed an intense absorption band at 428 nm (Soret band) and less intense Q bands at 514 nm, 559 nm, 597 nm, and 647 nm Table 3.1, similarly the unmetalated porphyrin **2**-H_2 of complexes **2**-Mn/**2**-Co showed a Soret band at 422 nm and four Q bands at 515 nm, 549 nm, 588 nm, and 642 nm. Upon the formation of the metalated complex **1**-Mn, **2**-Mn, and **2**-Co, the four Q bands in free base porphyrins collapsed into two and the Soret bands red shifted to 483 nm, 476 nm, and 444 nm, respectively, Table 3.1. The presence of manganese metal in complex **1**-Mn and **2**-Mn was also easily detected by the presence of the bands between 350 nm and 435 nm which are typical of Mn porphyrins and are assigned to charge transfer transitions [67]. Soret band is red shifted for **1**-Mn compared to **2**-Mn due to NH_2 which are electron donating groups. The GQDs showed a sharp absorption band at 334 nm similar to literature

reports [68]. In the presence of GQDs, the porphyrin Soret band blue shifts, an indication of a strong interaction between GQDs and porphyrin [69]. A blue shift in the Soret band was observed upon attaching (covalently) complex **1**-Mn to GQDs to form **1**-Mn@GQDs (477 nm). Similar trends were observed upon the formation (π- π stacking) of **1**-Mn--GQDs (480 nm), **2**-Mn--GQDs (473 nm), and **2**-Co--GQDs (439 nm) respectively. This is an indication that the linkage was successful, Table 3.1.

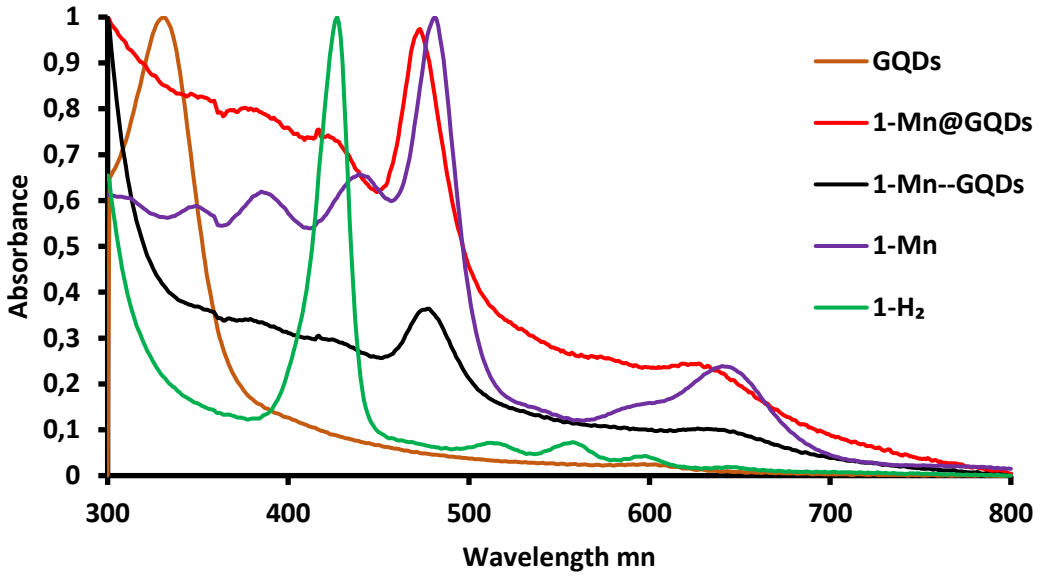

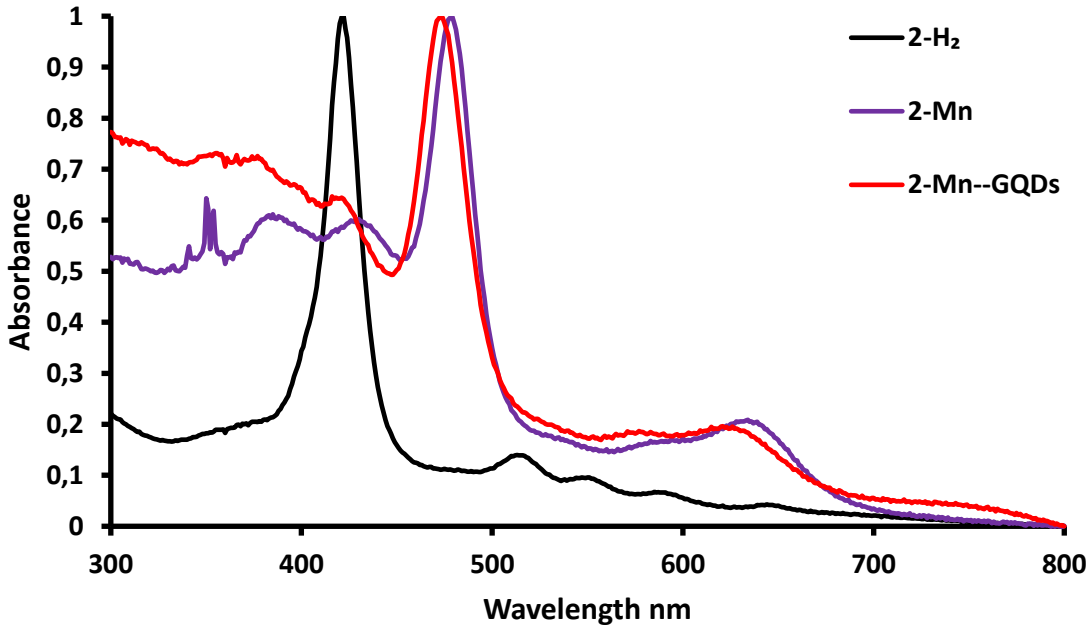

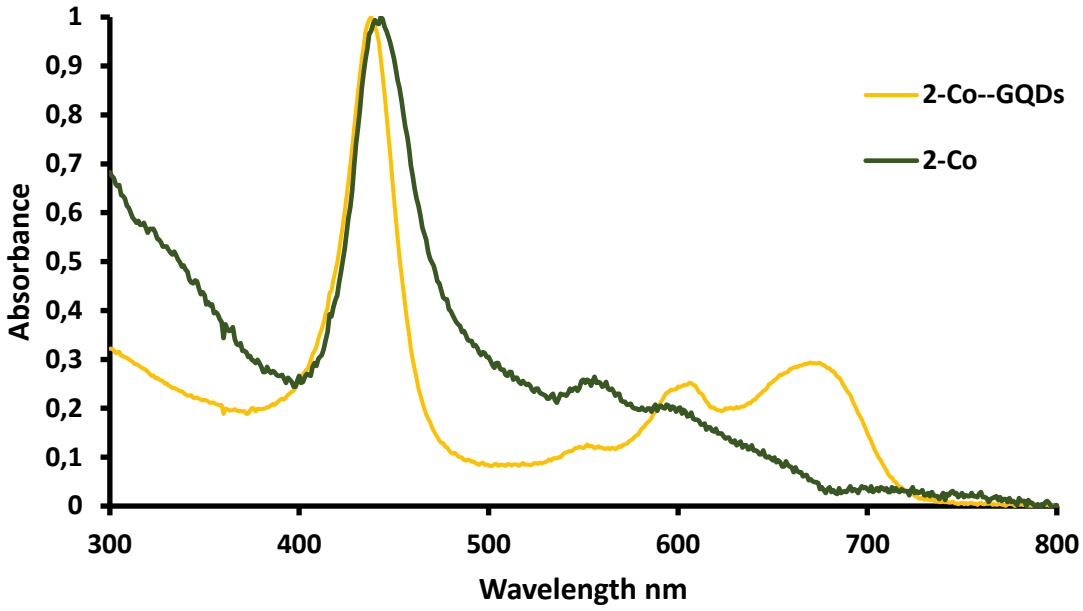

Fig. 3.2. UV-visible spectra of all complexes used in this thesis, all in DMF except GQDs which is in water.

Table 3.1. UV-vis electronic absorption spectral data, in DMF unless otherwise stated.

Sample	Soret (nm)	Q bands (nm)
GQDs	-	-
1-H_2	428	647,597,559,514
1-Mn	483	646,589
1-Mn--GQDs	480	640,571
1-Mn@GQDs	477	631,575
2-H_2	422	515,549,588,642
2-Co	444	557,599
2-Mn	476	581,635
2-Co--GQDs	439	551,602,673
2-Mn--GQDs	473	579,626

GQDs UV band @ 334 nm in water.

3.3 Dynamic light scattering (DLS) and transmission electron microscopy (TEM)

Dynamic light scattering (DLS) measurements were carried out to determine the hydrodynamic sizes of the GQDs and composites Fig. 3.3. The hydrodynamic size for GQDs was found to be 6.50 nm, Table 3.2. After combining the metal porphyrin with GQDs, the hydrodynamic size of **1**-Mn--GQDs, **1**-Mn@GQDs, **2**-Mn--GQDs, **2**-Co--GQDs was found to be 32.68 nm, 31.69 nm, 15.70 nm, and 18.20 nm, respectively with a standard deviation of 11.61. Thus, there was an increase in size compared to the size of GQDs alone. TEM images and size distribution of GQDs and their combination with metal porphyrin are shown in Fig. 3.4. The size for GQDs was found to be 4.28 nm, there was a size increase after combining with metal porphyrins. Looking at the TEM images, the size increase could be due to aggregation [70]. DLS sizes are normally larger in comparison to those determined by TEM since DLS tends to be skewed towards larger particles [71].

Table 3.2. DLS and TEM sizes in DMF unless otherwise stated.

Sample	**DLS (nm)**	**TEM (nm)**
GQDs	6.5	4.28
1-H_2	-	-
1-Mn	-	-
1-Mn--GQDs	32.68	30.01
1-Mn@GQDs	31.69	30.33
2-H_2	-	-
2-Co	-	-
2-Mn	-	-
2-Co--GQDs	18.20	-
2-Mn--GQDs	15.70	-

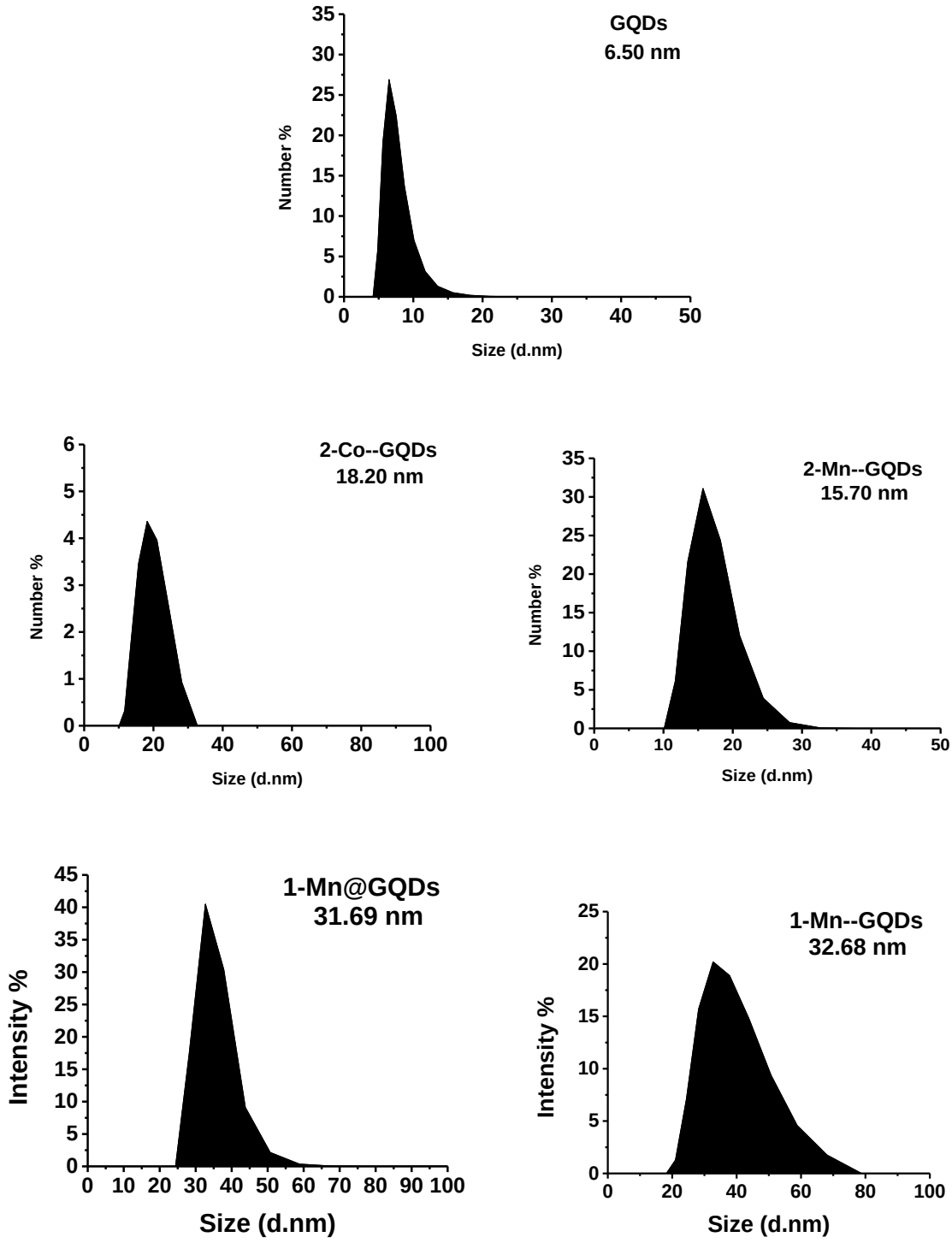

Fig. 3.3. DLS illustration of the average size of GQDs and complex **1**-Mn@GQDs, **1**-Mn--GQDs, **2**-Mn--GQDs, and **2**-Co--GQDs.

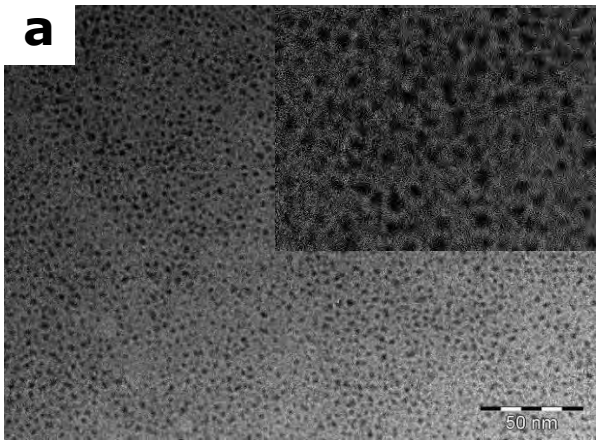
a
50 nm

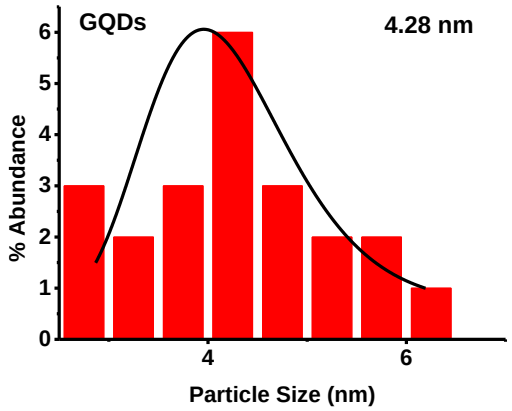
GQDs
4.28 nm
% Abundance
Particle Size (nm)

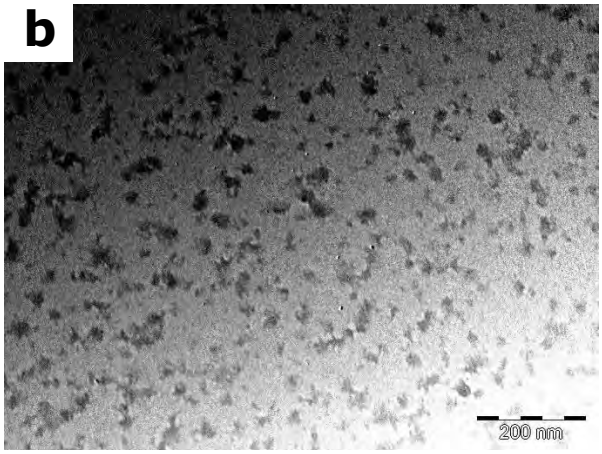
b
200 nm

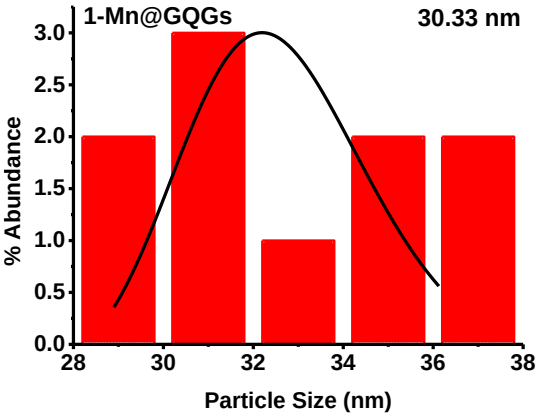
1-Mn@GQGs
30.33 nm
% Abundance
Particle Size (nm)

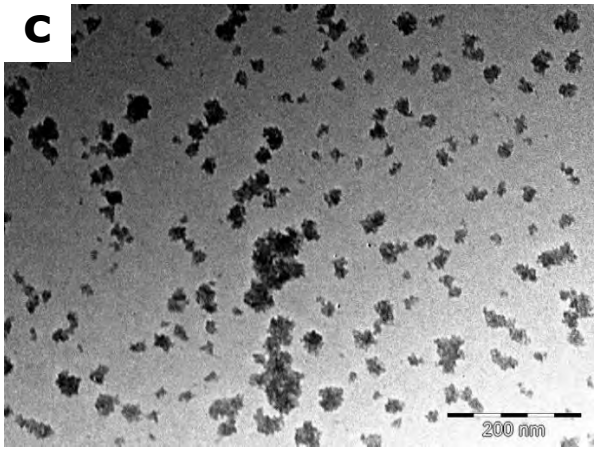
c
200 nm

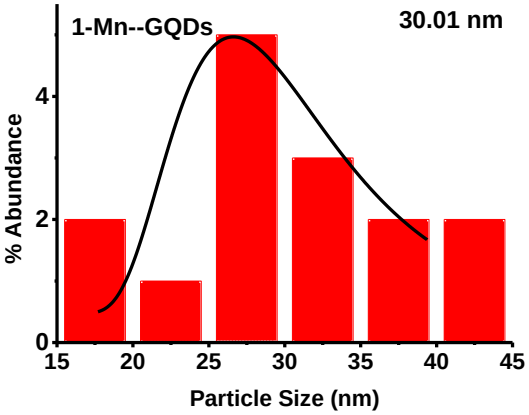
1-Mn--GQDs
30.01 nm
% Abundance
Particle Size (nm)

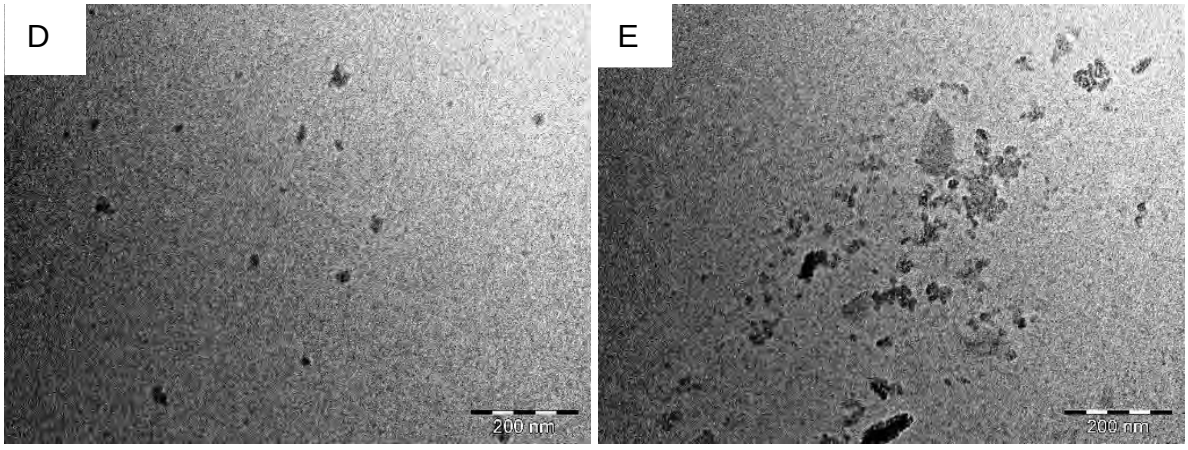

Fig. 3.4. TEM images of a) GQDs, b) **1**-Mn@GQDs, c) **1**-Mn--GQDs, d) **2**-Mn--GQDs, e) **2**-Co--GQDs, and corresponding histogram.

3.4 X-ray diffraction (XRD) patterns and energy dispersive spectroscopy (EDS)

XRD patterns of all complexes used are shown in Fig. 3.5. A broad peak at $2\Theta = 20^{o}$ was obtained from the XRD analysis of GQDs which is due to (002) Bragg's reflection of the carbon in the graphene layers [72]. Complex **1**-Mn displayed broad peaks that are typical of porphyrins [73]. Surprisingly sharp peaks between $2\Theta = 12^{o}$ and $2\Theta = 50^{o}$ were observed for complex **2**-Co and **2**-Mn which represents the crystallinity of the metal porphyrins. For these complexes the XRD experiments were carried as follows: two drops of DMF were added into the porphyrin to make a paste, as opposed to the others which were directly loaded as solid/powder on the plate. Solvated porphyrins result in aggregation which may in turn result in self assembled aggregation. Solvated porphyrins have elements of crystallinity [74]. Upon linking, the broad peaks of GQDs and **1**-Mn are observed with a slight shift. Similarly, the sharp peaks from **2**-Co were still observed after combining with GQDs but reduced in intensity, indicating the presence of both GQDs and **2**-Co. However, the sharp peaks from **2**-Mn were not observed after combining with GQDs. The speculation is that the crystallinity of **2**-Mn changes after combining with GQDs and this could be due to the presence of the axial ligand which limits the aggregation [75]. A shift in the amorphous peak of GQDs was observed after combining with both porphyrins indicating the presence of the metal porphyrin and GQDs [76].

The elemental composition of the synthesized complexes (**1**-Mn, **2**-Mn, **2**-Co, GQDs, **1**-Mn--GQDs, **1**-Mn@GQDs, **2**-Co--GQDs, and **2**-Mn--GQDs.) was determined using energy dispersive X-ray spectroscopy. The results obtained were consistent with the expected elemental composition Fig. A2 (Appendix), for a section of EDS spectra.

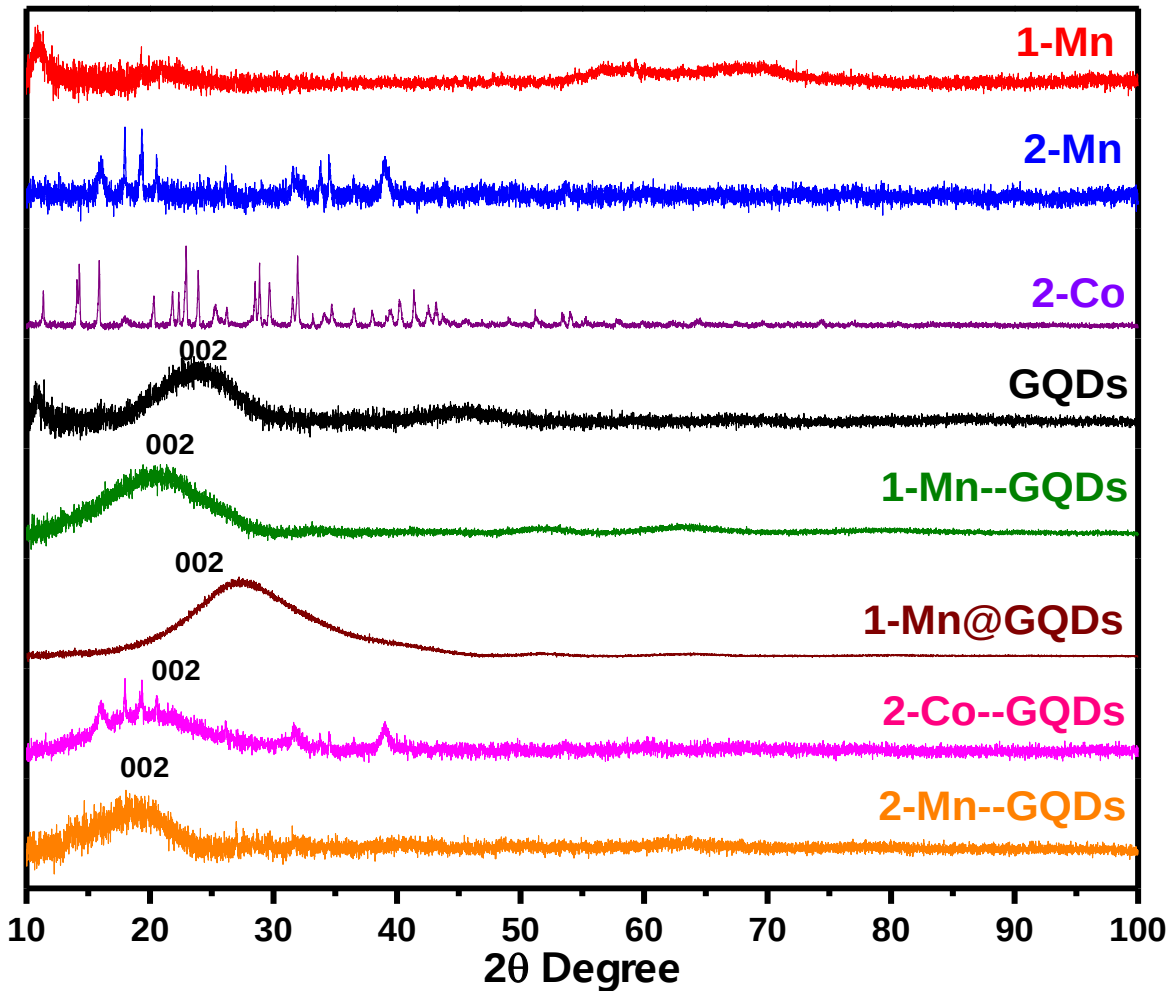

Fig. 3.5. XRD spectra of **1**-Mn, **2**-Mn, **2**-Co, GQDs, **1**-Mn--GQDs, **1**-Mn@GQDs, **2**-Co--GQDs, and **2**-Mn--GQDs.

3.5 X-ray photoelectron spectroscopy (XPS) studies

X-ray photoelectron spectroscopy was used to confirm the amide linkage between **1**-Mn and GQDs to give **1**-Mn@GQDs Fig. 3.6. The high-resolution spectrum N1s was deconvoluted into two components at 397.4 eV and 399.3 eV corresponding to N-C and NH_2 for **1**-Mn, Fig. 3.6. N1s deconvolution for **1**-Mn@GQDs also yielded two peaks at (398.2 eV) and (399.1 eV) corresponding to N-C and NH-C(O) which confirmed the binding of carbonyl and the nitrogen

forming amide bond [77]. There are no differences in high resolution N1s XPS spectra for the non-covalently attached **1**-Mn--GQDs compared to **1**-Mn since there are no new bonds.

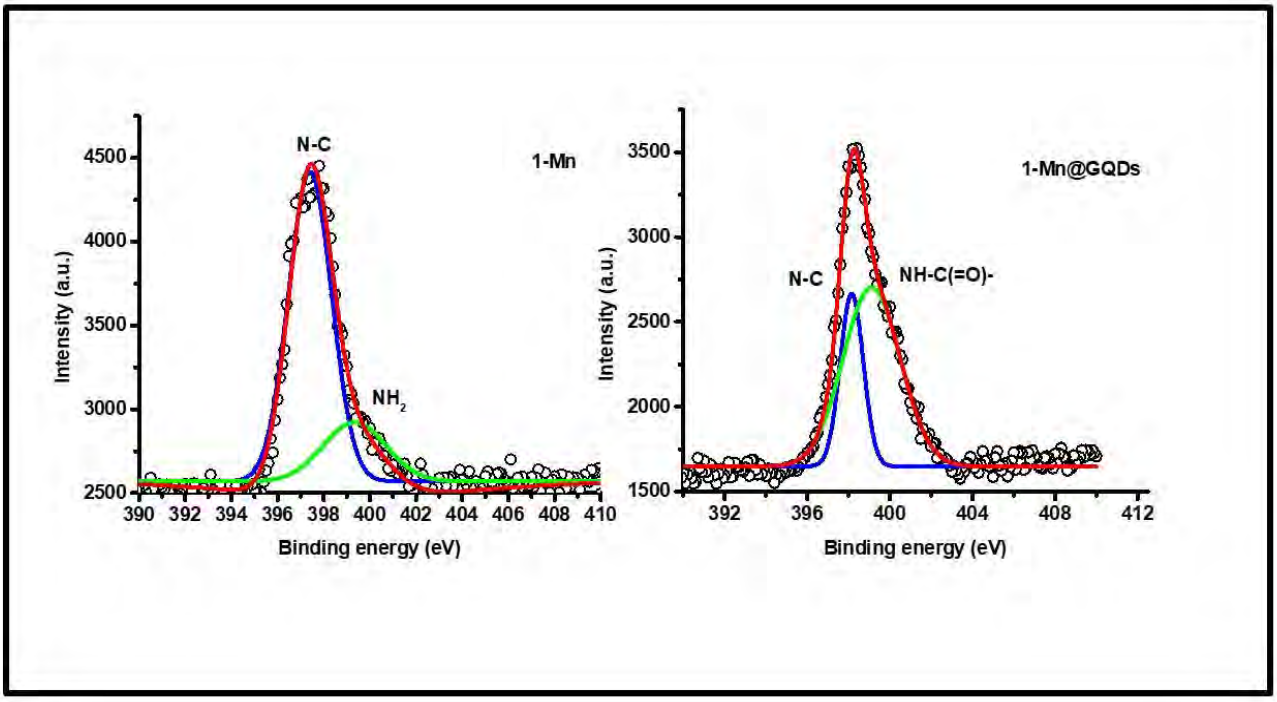

Fig. 3.6. XPS high resolution N1s of **1**-Mn and **1**-Mn@GQDs.

3.6 Conclusions

DLS, TEM, and XRD confirmed the synthesis of GQDs. The synthesis of complex **2**-Co/**2**-Mn was successful as confirmed by the UV-vis spectra. The Soret band for complex **2**-Mn was more blue shifted compared to complex **1**-Mn due to the presence of NH_2 group in the latter. XPS results showed successful combination of metal porphyrin and GQDs by forming an amide bond after conjugation.

Chapter 4:

Electrode modification and characterization

This chapter covers the characterization of the modified electrodes in buffer and in ferrocyanide-ferricyanide solution.

4. Characterization of Modified Electrode

4.1 Characterization in ferricyanide solution

4.1.1 Cyclic voltammetry (CV)

All the GCE electrodes were modified using drop-dry method as described in chapter 2. The modified electrodes were characterized using cyclic voltammetry (CV). Ferrocyanide-ferricyanide $[Fe(CN)_6]^{3-/4-}$ solution was used as a redox mediator due it its stability and high reversibility [78].

The CV scans of bare electrode of all probes in $[Fe(CN)_6]^{3-/4-}$ are shown in Fig. 4.1. The anodic and cathodic peak potential separation (ΔE_p) values are shown in Table 4.1. A peak separation ΔE_p closer to the Nernstian value 58 mV indicates a good electron transfer kinetics for the $[Fe(CN)_6]^{3-/4-}$ [79]. The bare electrode showed the smallest peak separation. The smaller the ΔE_p, the better the electron transfer. Thus, the bare electrode shows good electron transfer behavior. Of the modified electrodes, the unmetalated porphyrin, complex **1**-H_2 showed poor electron transfer kinetics with the highest ΔE_p value and complex **2**-Mn--GQDs showed the best electron transfer ability amongst the modified electrode with the lowest ΔE_p value.

In terms of the metalated porphyrins alone, complex **2**-Mn showed good electron transfer ability with smaller ΔE_p value followed by complex **2**-Co (both containing push-pull substituents) and **1**-Mn (tetra substituted) performed the worst. The best performing electrodes are those containing push-pull substituents. Push-pull substituents are known to enhance electron transfer properties [33].

GQDs showed better electron transfer ability compared to complexes **1**, with the lowest ΔE_p value of 276 mV as shown in Table 4.1.

For non-covalently liked (π-π stacking) composites, the electron transfer ability improved in the order: **2**-Mn--GQDs > **2**-Co--GQDs > **1**-Mn--GQDs. The best electron transfer came from the electrodes containing complex **2**-Mn and **2**-Co (**2**-Mn--GQDs and **2**-Co--GQDs) which both contain push-pull substituents. Furthermore, the addition of GQDs improved the electron transfer ability in all the composites. The covalently linked composite showed slightly poor electron transfer compared to all the non-covalently linked composites. However, this has no bearing on the electrochemical activity of a porphyrin in response to an analyte under study, as will be discussed below. As no bond formation takes place, non-covalent interaction

preserves GQDs electronic properties, hence better electron transfer. It is also noted that complex **2**-Mn has better electron transfer ability than **2**-Co when alone or in the presence of GQDs, Mn has high ability to promote electron transfer [80].

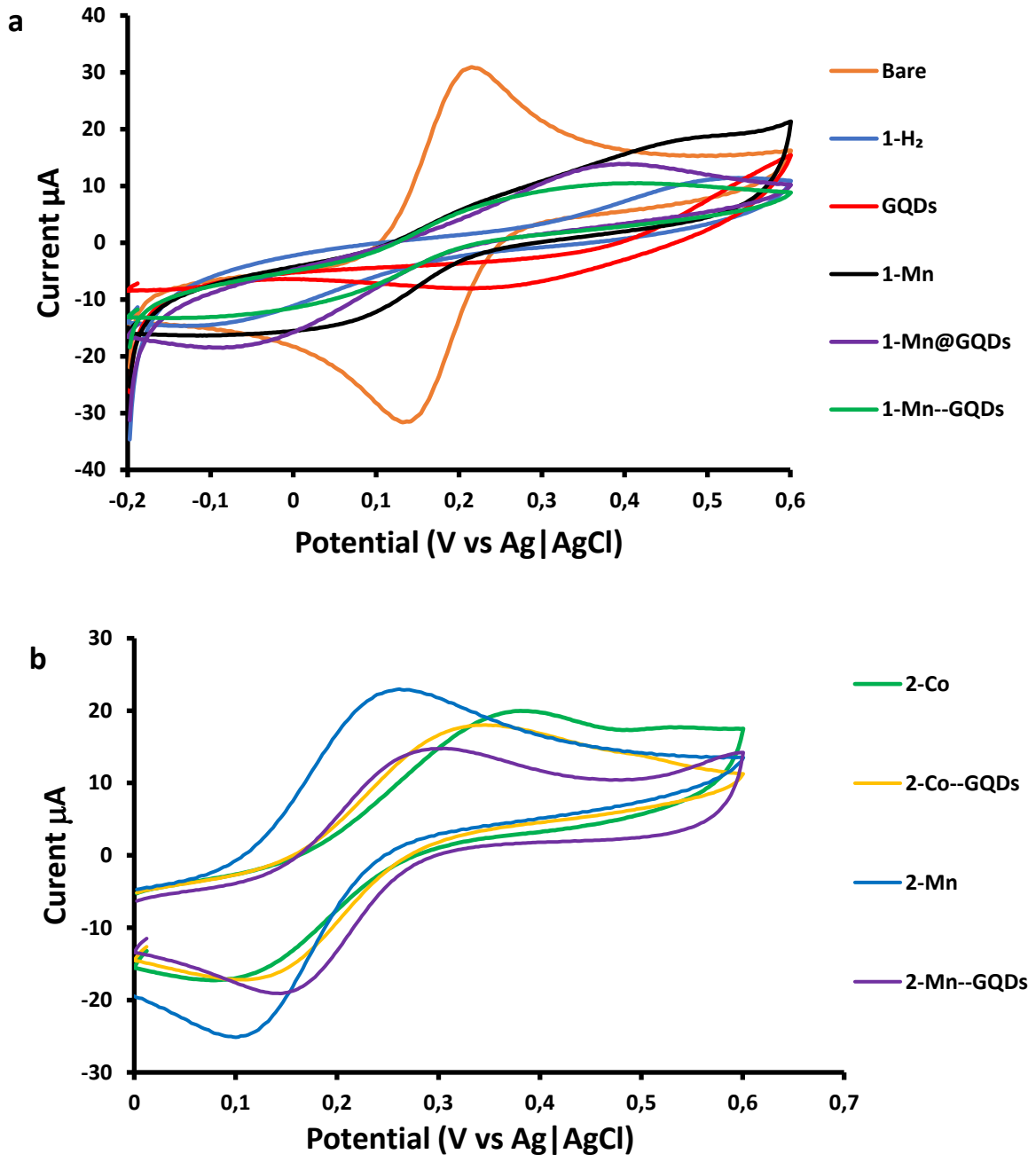

Fig. 4.1. Cyclic voltammograms of a) bare electrode, **1**-H_2, GQDs, **1**-Mn, **1**-Mn@GQDs, **1**-Mn--GQDs, b) **2**-Co, **2**-Co--GQDs, **2**-Mn, and **2**-Mn--GQDs at 100 mV/s in 1 mM $[Fe(CN)_6]^{3-/4-}$ in 0.1 M KCl.

Table 4.1. Electrochemical data on characterization of modified electrodes in 1mM $[Fe(CN)_6]^{3-/4-}$ in 0.1 M KCl.

Electrodes	**ΔE (mV) 1 mM $[Fe(CN)_6]^{3-/4-}$ in 0.1 M KCl.**	**Γ (mol.cm^{-2})**
Bare	69	-
GQDs	276	2.65×10^{-9}
1-H_2	517	2.79×10^{-10}
1-Mn	414	1.61×10^{-7}
1-Mn@GQDs	371	1.09×10^{-7}
1-Mn--GQDs	324	1.51×10^{-7}
2-Co	231	2.88×10^{-7}
2-Mn	150	1.83×10^{-7}
2-Co--GQDs	187	4.55×10^{-8}
2-Mn--GQDs	124	5.89×10^{-8}

The active area of the electrode was determined using the Randles-Sevcik Eqn.4.1 and using $[Fe(CN)_6]^{3-/4-}$ in 0.1 M KCl.

$$I_p = 2.69 \times 10^5 n^{3/2} ACD^{\frac{1}{2}} v^{1/2} \qquad (4.1)$$

Where I_p= is the peak current, A= the effective surface area, C= concentration of $[Fe(CN)_6]^{3-/4}$, D= diffusion coefficient 7.6×10^{-6} cm^2/s of $[Fe(CN)_6]^{3-/4}$ [81], n= the number of electrons involved, and v= scan rate. The calculated areas from Eqn.4.1 were found to be 0.097 cm^2, 0.085 cm^2, 0.078 cm^2, 0.076 cm^2, 0.061 cm^2, 0.058 cm^2, 0.044 cm^2, 0.042 cm^2 and 0.040 cm^2 for **2**-Mn, **2**-Co, **1**-Mn, **2**-Co--GQDs, **2**-Mn--GQDs, **1**-Mn@GQDs, **1**-Mn--GQDs, **1**-H_2, and GQDs respectively. These will be employed below for calculations of surface coverage.

4.1.2 Electrochemical impedance spectroscopy (EIS)

Electrochemical impedance spectroscopy (EIS) was used to study the redox structural features of the modified surface of the electrode. The Nyquist plots provided in Fig. 4.2 are used to study the impedance behavior [82]. The electrochemical response of each electrode is recorded in terms of R_{ct}. The R_{ct} value is a measure of electron transfer resistance on an electrode. The R_{ct} values obtained via Randles model (Fig. 4.2c.) are provided in Table 4.2. The lower the R_{ct} value the better the charge transfer kinetics, bare showed the lowest. **1**-Mn gave lower Rct value compared to **1**-H_2 due to the presence of manganese, moreover both **1**-Mn--GQDs and **1**-Mn@GQDs gave lower Rct values compared to **1**-Mn due to the incorporation of GQDs. Furthermore **1**-Mn--GQDs gave a slightly lower Rct value compared to **1**-Mn@GQDs.
In the case of the push-pull substituted porphyrin and their composites, the R_{ct} values obtained are as follows, **2**-Mn--GQDs (3.99 KΩ), **2**-Mn (7.28 KΩ), **2**-Co--GQDs (8.02 KΩ) and **2**-Co (9.45 KΩ), Table 4.2. **2**-Mn showed better conductivity than **2**-Co. Of all the modified electrodes, **2**-Mn--GQDs showed the best charge transfer kinetics with the lowest R_{ct}. Moreover, introduction of GQDs to **2**-Co and **2**-Mn lowered the R_{ct} which improved the charge transfer kinetics. The EIS results correspond to peak separation ΔE_p which also indicates electron transfer kinetics for each set of **1** or **2** complexes.

Table 4.2. The Rct values of bare and modified electrodes in 1mM $[Fe(CN)_6]^{3-/4-}$ in 0.1 M KCl.

Electrodes	**R_{ct} (kΩ)**
Bare	0.09
GQDs	0.19
1-H_2	3.14
1-Mn	0.86
1-Mn@GQDs	0.39
1-Mn--GQDs	0.26
2-Co	9.45
2-Mn	7.28
2-Co--GQDs	8.02
2-Mn--GQDs	3.99

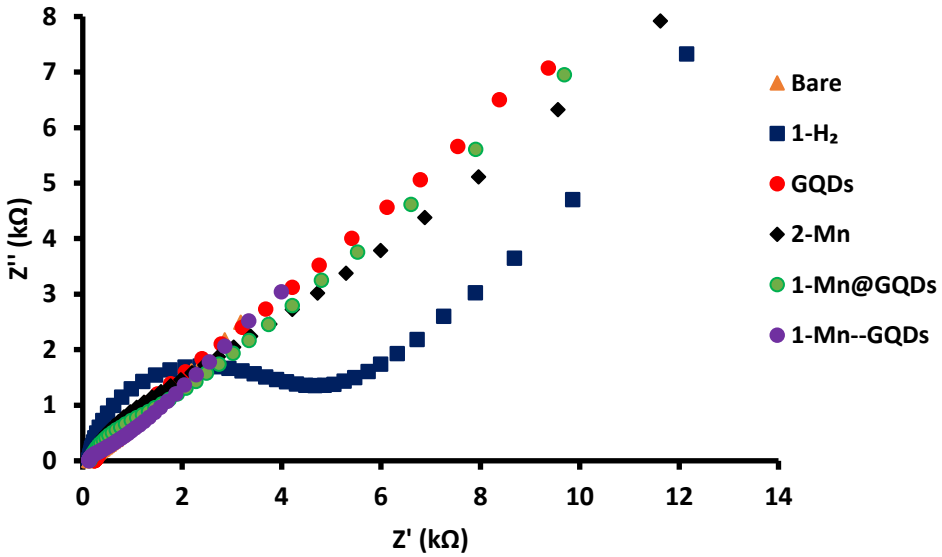

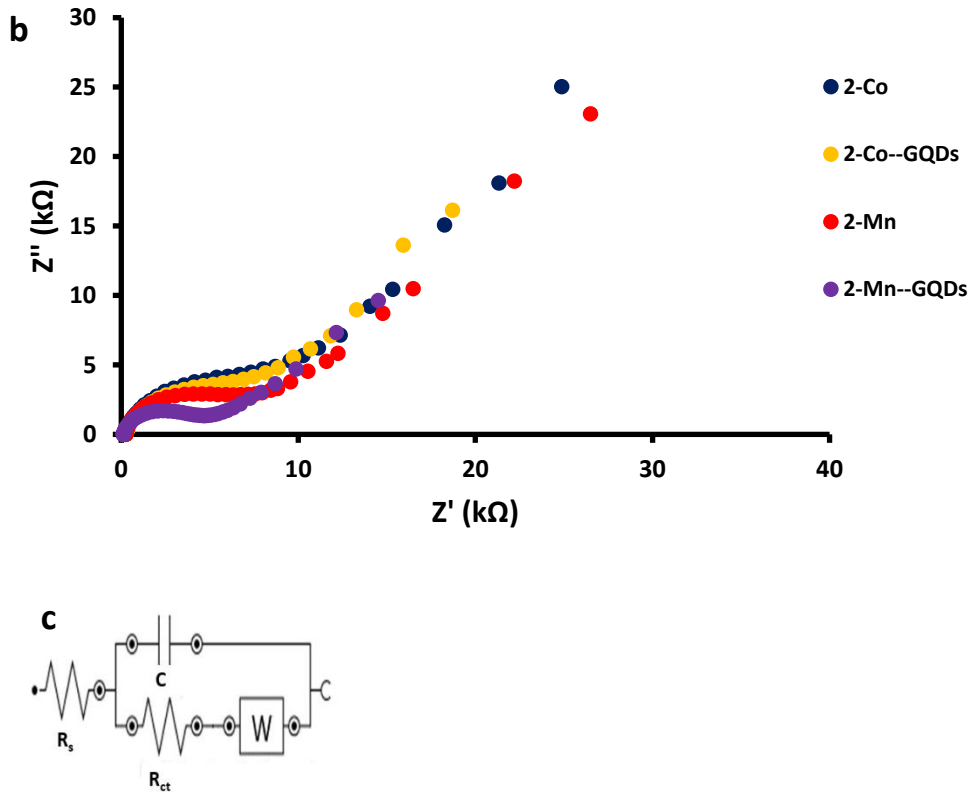

Fig. 4.2. a) Nyquist plots of bare and modified electrodes: a) bare, **1**-H_2, GQDs, **1**-Mn, **1**-Mn@GQDs, and **1**-Mn--GQDs. b) **2**-Co, **2**-Co--GQDs, **2**-Mn, and **2**-Mn--GQDs in 1 mM $[Fe(CN)_6]^{3-/4-}$ in 0.1 M KCl. c) Randles model used for fitting.

4.2 Characterization in 0.1M NaOH buffer

Fig. 4.3. shows the cyclic voltammograms of bare and modified electrodes in 0.1 M NaOH (to be used for the detection of analyte) in the absence of analyte. The purpose of this experiment is to distinguish the activity of the electrocatalysts in the presence and absence of the analyte. Peaks observed from 0.3 V to 0.7 V for all porphyrin containing electrodes are due to the porphyrin ring since Mn(III) porphyrins do not show metal oxidation [83,84]. Peaks between -0.3 V and -0.5 V are due to (Mn(III)/Mn(II) processes) for MnP. The peaks between -0.3 V and -0.5 V are attributed to Co(ll)/Co(l) in CoP. The peaks were also observed in the presence of GQDs but were reduced in intensity due to the covering of the metal porphyrin by GQDs. In addition, GQDs alone showed a peak near -0.4 V which was expected for GQDs [85]. Fig. A3 (Appendix) shows GQDs, **1**-Mn, and **1**-Mn@GQDs CV at a smaller potential

window (-0.8 V to +0.8 V) to avoid the signals from oxygen evolution reaction (OER) as it is normally detected around +0.8 V and above. There is no OER effect in Fig. A3. The peaks observed at the negative potentials between -0.3 V and -0.5 V were employed for the determination of surface coverage Eqn. 4.2.

$$\Gamma = \frac{\boldsymbol{Q}}{\mathbf{nFA}} \qquad (4.2)$$

where Q is the integrated effective area of the electrode, n the number of electrons transferred, F the Faraday constant (96,485 C mol^{-1}), A is the effective surface area obtained from Eqn. (4.1) and Γ is the surface coverage. The surface coverage values are presented in Table 4.1. The **1**-Mn--GQDs showed higher surface coverage compared to **1**-Mn@GQDs and **1**-H_2 showed the lowest surface coverage compared to all probes. It has been reported that low surface coverage limits charge density and the electron transfer depends on it [86]. An increase in surface coverage increases electron transfer rate. **2**-Co showed higher surface coverage compared to **2**-Mn. Surface coverage reduced after introducing GQDs in all complexes indicating that GQDs is negatively affecting the electron transfer rate. This could be due to aggregation of GQDs loaded to the porphyrin.

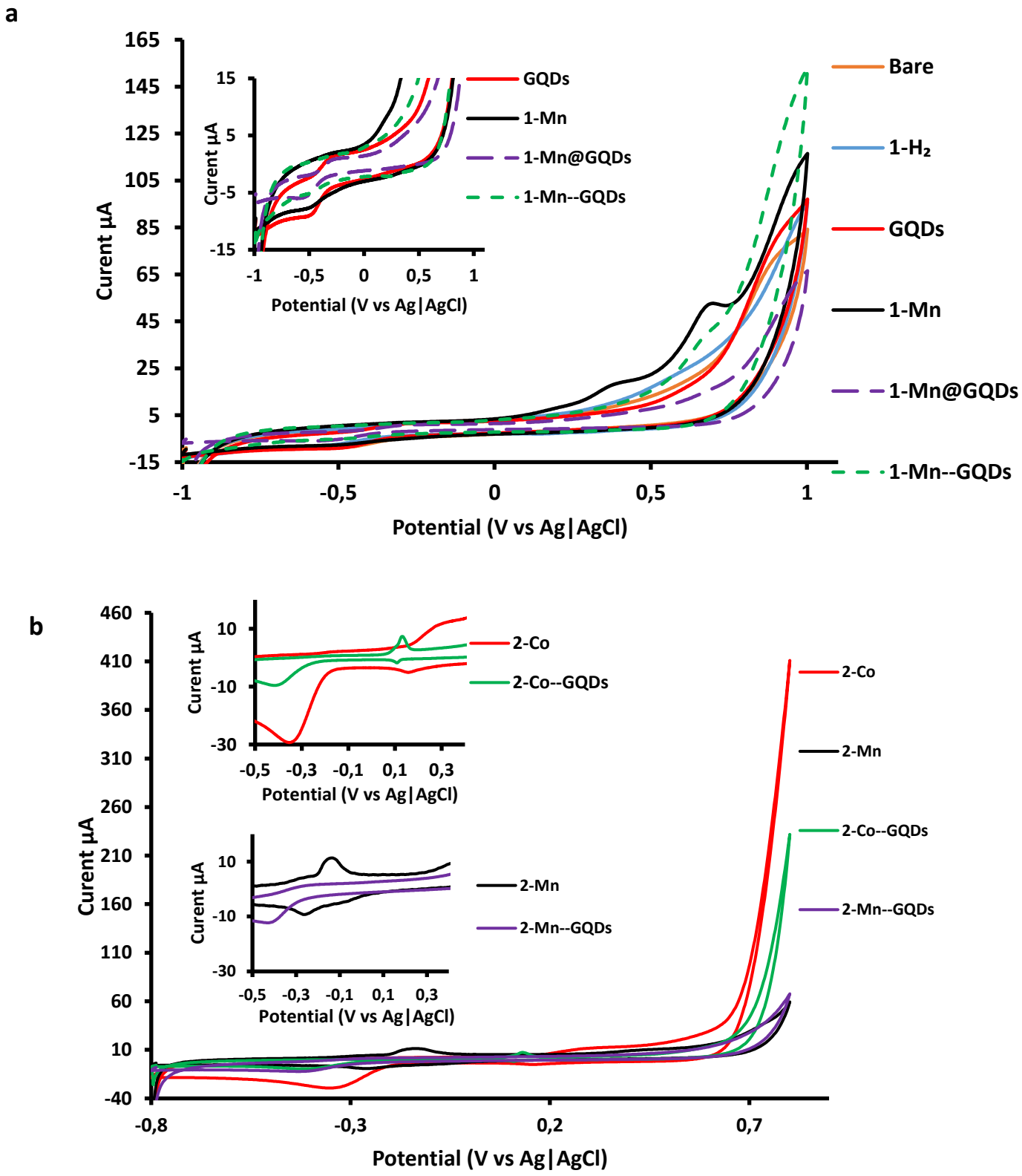

Fig. 4.3. Cyclic Voltammograms of bare and modified electrodes, a) bare electrode, **1**-H_2, **1**-Mn, GQDs, **1**-Mn@GQDs, and **1**-Mn--GQDs, insert: expansion to show peaks near -0.5 V better. b) **2**-Co, **2**-Mn, **2**-Co--GQDs, **2**-Mn--GQDs, insert: expansion to show peaks between +0.3 V and -0.5 V. All at 100 mV/s in 0.1 M NaOH.

4.3 Conclusions

The electrode characterization confirmed the modification of the electrode surface. All the modified electrodes showed good surface coverage and effective area of the electrode. The introduction of GQDs showed improved electron transfer ability in all cases compared to porphyrin alone.

Chapter 5:

Electrocatalytic Detection of Hydrazine

This chapter studies the effect of porphyrin, manganese and cobalt porphyrin alone and in the presence of GQDs on electro-oxidation of hydrazine.

5. Electrocatalytic detection of Hydrazine

5.1 Cyclic voltammetry

The cyclic voltammetric responses of modified glassy carbon electrodes in NaOH buffer in the presence of hydrazine are shown in Fig. 5.1 using complexes **1** as examples. The anodic peak potential for the oxidation of hydrazine is observed but no cathodic peak is found, and this indicates irreversible behavior [87]. The peak potential observed ranged from 0.60 V to 0.80 V for the detection of hydrazine, Table 5.1. Hydrazine oxidation occurs at 0.75 V for **1**-H_2. A decrease of 0.10 V in peak potential with an increase in background current is observed in the presence of manganese as a central metal (**1**-Mn) and this therefore shows an improvement in electrocatalytic activity for the metalated complex [88]. The catalytic activity of porphyrin on electro-oxidation of hydrazine is determined by the central metal ion. The GQDs showed the anodic peak potential of 0.80 V while complex **1**-Mn@GQDs and **1**-Mn--GQDs showed 0.68 V and 0.70 V respectively under same conditions, giving a standard deviation of 0.064. Although the both **1**-Mn@GQDs and **1**-Mn--GQDs showed higher anodic peak potential compared to that of **1**-Mn, complex **1-**Mn@GQDs showed lower anodic peak potential (0.68 V) compared to **1**-Mn--GQDs (0.70 V) and this could be due to the effect of the direct linkage of GQDs and the porphyrin. According to the previous studies, GQDs result in shifting the potential to the negative direction and this is because GQDs have high electron transfer rate [89]. Complex **2**-Mn showed an oxidation peak potential at 0.60 V, this is lower potential compared to that of a manganese tetra substituted porphyrin **1**-Mn 0.65 V Table 5.1. The lowering of the oxidation peak potential is due to the presence of electron withdrawing and electron donating groups in the metal porphyrin.

Complex **1**-Mn--GQDs and **1**-Mn@GQDs showed the largest background corrected current in Table 5.1. **1**-Mn--GQDs showed slightly lower catalytic current compared to **1**-Mn@GQDs and this could be due to the aggregation of GQDs loaded to the porphyrin resulting in lower catalytic activity. High currents are more important as they play part in giving better limit of detection (LoD). **2**-Co showed a higher current compared to **2**-Mn. This could be due to the high active surface area of the electrode and the catalytic ability of **2**-Co. In the presence of GQDs, a decrease in anodic peak current in **2**-Co--GQDs was observed compared to **2**-Co, corresponding to a decrease in surface coverage (Table 4.1). However, the current was increased for **2**-Mn--GQDs compared to **2**-Mn, even though there was a decrease in surface

coverage. The introduction of GQDs is known to increase the catalytic current, the decrease in anodic peak current can be attributed to aggregation as observed in TEM (chapter 3).

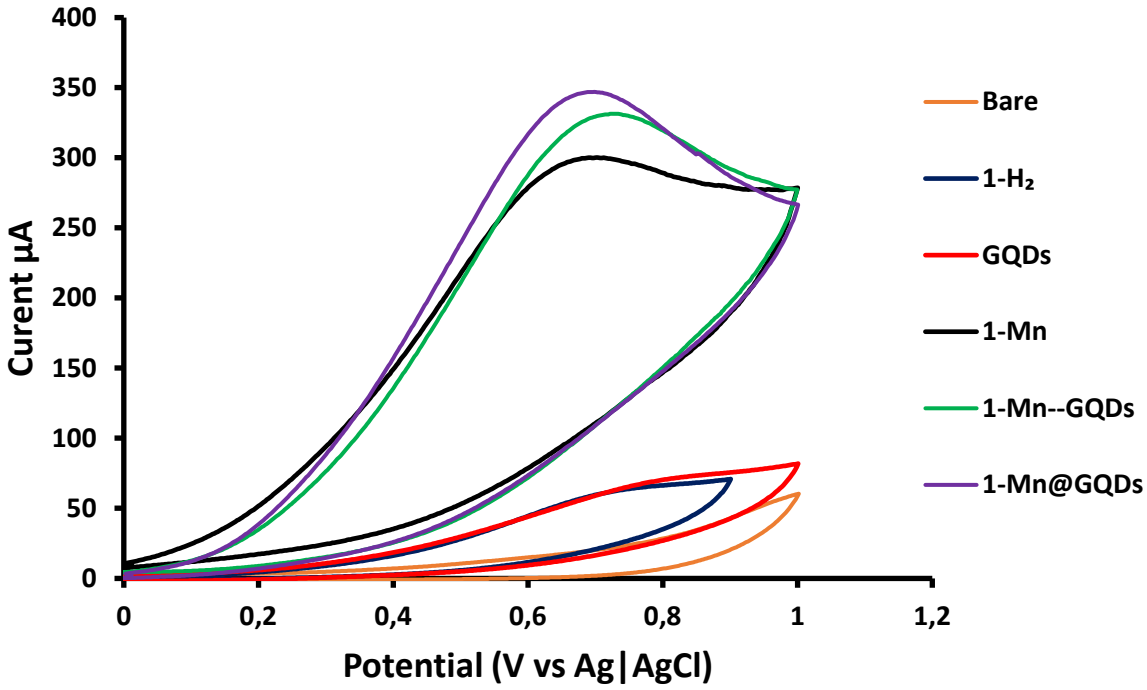

Fig. 5.1. Cyclic voltammograms of bare electrode, **1**-H_2, **1**-Mn, GQDs, **1**-Mn@GQDs, and **1**-Mn--GQDs at 100 mV/s in 0.1 M NaOH containing 1 mM Hydrazine.

The anodic oxidation of hydrazine in aqueous solution has been widely studied for several years [24-26]. The proposed mechanism (Eqs. 5.1-5.3) for hydrazine oxidation is similar to that reported for Mn phthalocyanines (Pc) [86] as follows, equations 5.1-5.3 (P = porphyrin).

$$Mn(III)P + N_2H_4 \rightarrow [Mn(II)P]^{-}....[N_2H_4]^{+} \quad (5.1)$$

$$[Mn(II)P]^{-}....[N_2H_4]^{+} + OH^{-} \leftrightarrow Mn(III)P....N_2H_3 + H_2O + e^{-} \quad (5.2)$$

$$Mn(III)P...N_2H_3 + OH- \rightarrow H_2O + Mn(III)P + N_2H_2 + e^{-} \quad (5.3)$$

Equation (5.3) is rate determining step.

It has been reported that N_2H_4 further decomposes rapidly via two one-electron steps to give N_2 which is the final product and also that Mn(III)P/Mn(II)P mediate the electrocatalysis of hydrazine [86]. The peaks related to Mn(III)P/Mn(II)P were observed in the supporting electrolyte NaOH as discussed in chapter 4.

The proposed mechanism for hydrazine oxidation is similar to the reported for CoPc [90] as follows, equations 5.4-5.7.

$$[Co(I)P]^{-}_{surface} \leftrightarrow [Co(II)P]_{surface} + e^{-} \quad (5.4)$$

$$[Co(II)P]_{surface} + N_2H_4 + OH^{-} \xrightarrow{rds} [Co(I)P \dots N_2H_3]^{-}_{surface} + H_2O \quad (5.5)$$

$$[Co(I)P \dots N_2H_3]^{-}_{surface} \rightarrow [Co(I)P]^{-}_{surface} + *_{N_2H_3} \quad (5.6)$$

$$*_{N_2H_3} + 3OH^{-} \xrightarrow{fast} + N_2 + 3e^{-} + 3H_2O \quad (5.7)$$

Eqn. 5.5 is the rate determining step. The symbol * indicates a radical specie. The mechanism of catalysed hydrazine electro-oxidation by MN4 macrocyclic complexes (metal-porphyrin and metal-phthalocyanine-like molecules) is strongly dependent on the nature of the metal and ligand and involves the transfer of four electrons to produce N_2 [91]. Hence different mechanisms.

The stability of all the complexes was tested by running 26 consecutive scans in 1 mM hydrazine Fig. 5.2 using complexes **1** as examples. There was only a small shift in potential but no decrease in current. The current stabilized after 26 consecutive scans. The metal porphyrin **1**-Mn showed better stability than **1**-H_2 whereas both **1**-Mn@GQDs and **1**-Mn--GQDs showed great results in stability. The electrodes were stored for 2 weeks and still showed stability.

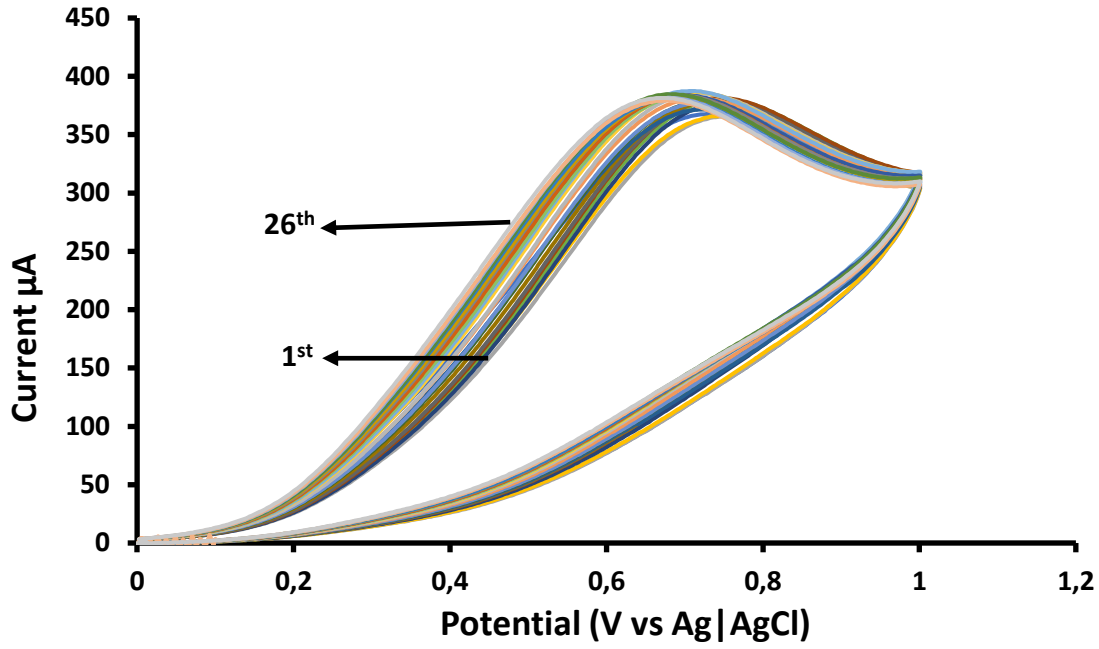

Fig. 5.2. Stability scans of **1**-Mn@GQDs at 100 mV/s in 0.1 M NaOH containing 1 mM hydrazine.

5.2 Kinetic studies of Hydrazine detection

Various scan rates were performed for the detection of hydrazine to determine the reversibility of the catalytic reaction Fig. 5.3a using **1**-Mn@GQDs as an example. The effect of scan rates on peak current of hydrazine oxidation at different platforms was monitored by plotting peak current as a function of square root of scan rates and is shown in Fig. 5.3c. The linear relationship between the current and the square root of scan rates indicates diffusion control [31,92-94]. Linear plots of Ep vs. Log v (Fig. 5.3b) were obtained and used to calculate Tafel slope with the help of Eqn.5.8.

$$E_p = \frac{b}{2}\log v + K \qquad (5.8)$$

where Ep is the potential, b is the Tafel slope, v is scan rate, and K is a constant. The Tafel slopes obtained for all the complexes are shown in Table 5.1. The Tafel slopes were all beyond the normal range (60-120 mV/decade). Tafel slopes that are higher than the 120 mV/decade

have no kinetic meaning and could be due to chemical complications in the reaction [94]. This indicates that the overall reaction mechanism is not simple most likely due to the presence of various reactive species on electrode surface.

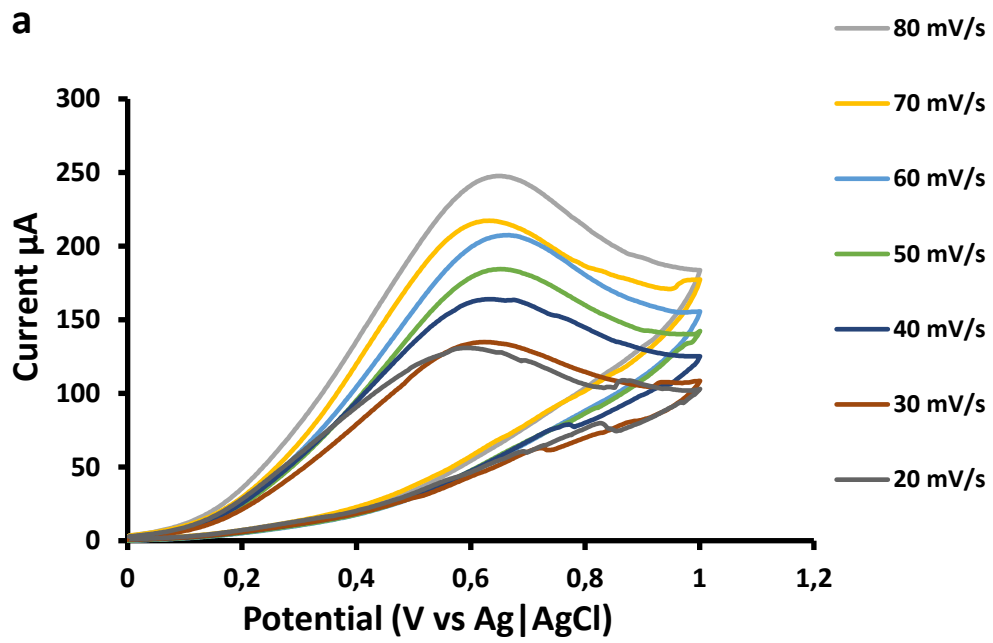

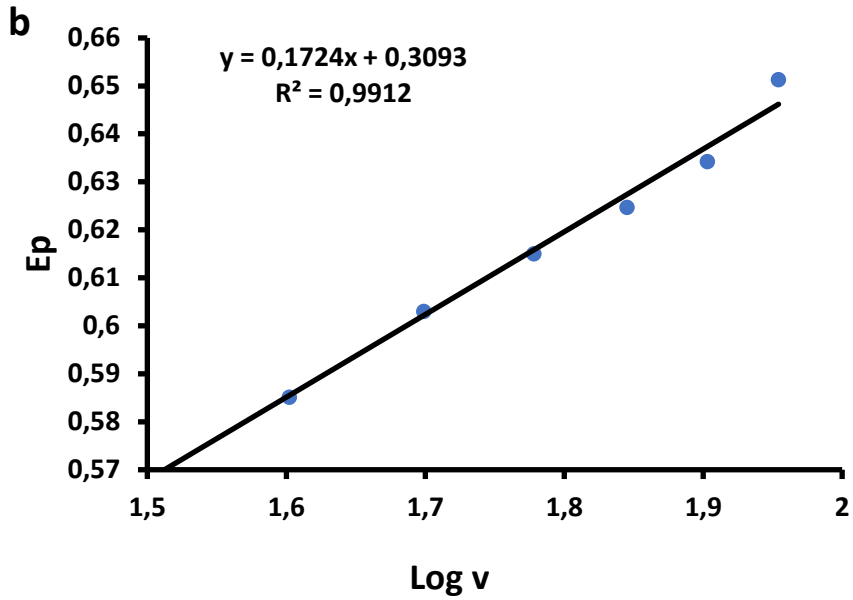

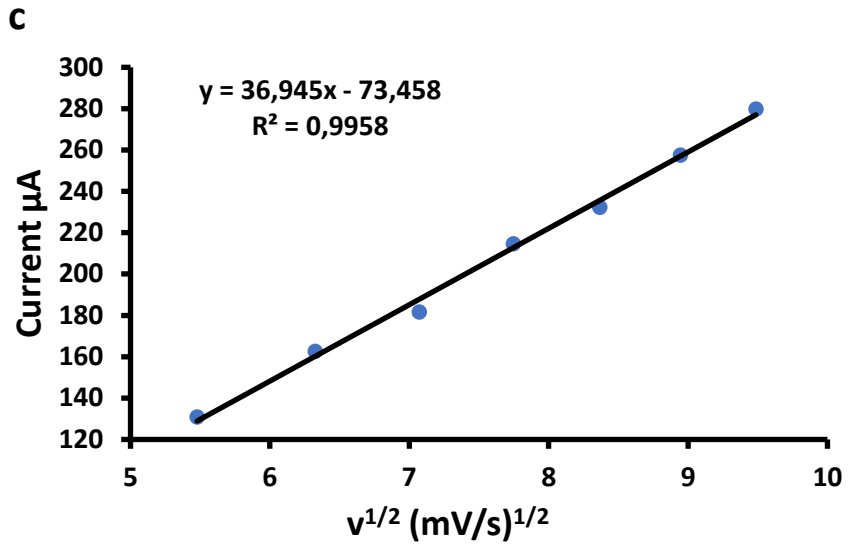

Fig. 5.3. (a) Cyclic voltammograms at various scan rate on **1**-Mn@GQDs, (b) plot of potential vs. log v and (c) plot of current vs. square root scan rate ($v^{1/2}$) in 1 mM hydrazine in 0.1 M NaOH.

Since Tafel slope values were all higher than the normal theoretical value 120 mV/decade. The adsorptive linear sweep voltammetry technique theory was employed to investigate their degree of adsorption (**2**-Co--GQDs was used as an example in Fig. 5.4). Fig. 5.4a shows linear sweep voltammetric evolution obtained at different concentrations of hydrazine. The linear sweep voltammetry was analyzed using the Langmuir adsorption isotherm theory [95].

$$\frac{[N_2H_4]}{I_{cat}} = \frac{1}{\beta I_{max}} + \frac{[N_2H_4]}{I_{max}} \qquad (5.9)$$

where I_{cat} is catalytic peak current in Fig. 5.4a for different concentrations at the peak potentials, I_{max} is maximum current obtained from the slope of $[N_2H_4]/I_{cat}$ Vs. $[N_2H_4]$ in Fig. 5.4b and β is the adsorption equilibrium constant which is related to electrochemical Gibbs free energy change (ΔG^o) by Eqn. 5.10 [95].

$$\Delta G° = -RT \ln \beta \qquad (5.10)$$

where R is the ideal gas constant, T is the absolute temperature. From the slope and the intercept in Fig. 5.4b, the β value was obtained and then used to estimate the ΔG^o value. The ΔG^o value was found to be -16.70 kJ mol^{-1}. The negative value indicates that the adsorption of hydrazine on **2**-Co--GQDs is a spontaneous process which justifies the larger Tafel slopes [96].

a

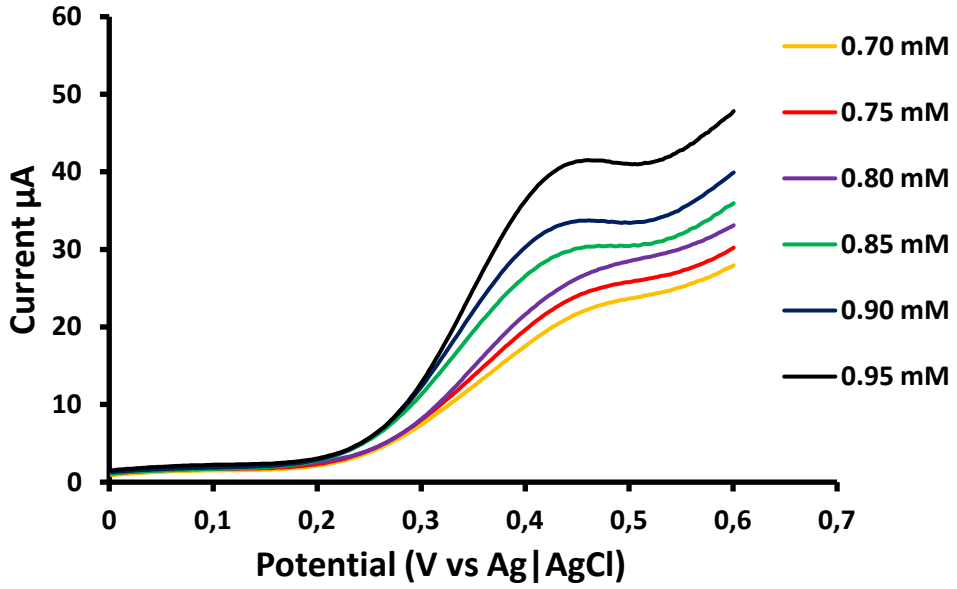

b

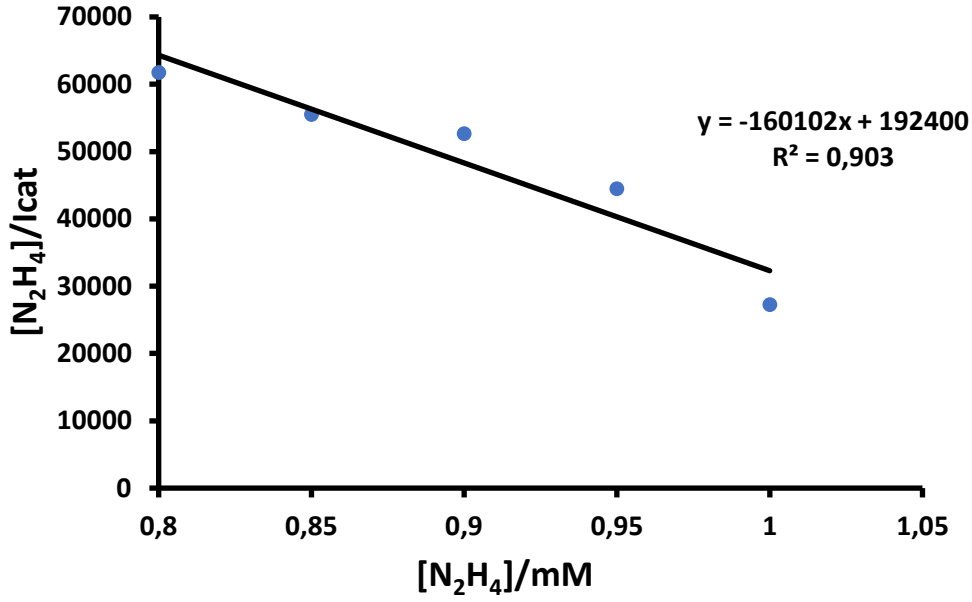

Fig. 5.4. (a) Linear sweep voltammetry of **2**-Co--GQDs at various concentrations (0.70 - 0.95 mM) (b) Langmuir adsorption isotherm plot for **2**-Co--GQDs.

Table 5.1. Electrochemical parameters of the modified electrodes

Complex	Tafel Slope (mV/dec)	Ep Hydrazine in 0.1 M NaOH	Background correct current (μA)	LoD (mM)	Catalytic rate (Ms^{-1})	Ref
Bare	-	-	-	-	-	This work
1-H_2	444	0.75	40	0.017	1.87×10^1	This work
1-Mn	657	0.65	278	0.011	1.83×10^2	This work
GQDs	319	0.80	46	0.018	5.99×10^1	This work
1-Mn@GQDs	344	0.68	321	0.0023	4.36×10^2	This work
1-Mn--GQDs	740	0.70	314	0.0042	1.94×10^2	This work
2-Co	209	0.68	233	0.0052	2.63×10^2	This work
2-Mn	378	0.60	116	0.013	4.89×10^1	This work
2-Co--GQDs	254	0.66	210	0.0025	6.39×10^2	This work
2-Mn--GQDs	328	0.63	144	0.0033	8.18×10^1	This work
(RGO/Au-TPP)[a]	-	0.47	-	0.003	-	[97]
(RGO^{III}/Pt-$TPPNc^{II}$)[b]	-	0.17	-	0.005	-	[98]
(GC-Co^{II}-OEP)[c]	-	0.35	-	0.051	-	[26]

Where a= tetra phenyl porphyrin/reduced graphene oxide, b= Ruthenium oxide nanocomposite and c= Cobalt Octaethylporphyrin

5.3 Chronoamperometric studies

Chronoamperometry was employed to determine the catalytic rate constant and the limit of detection (LoD) of the complexes. Fig. 5.5a shows the chronoamperogram of **1**-Mn@GQDs as an example. Plots of I_{cat}/I_{buf} vs. square root of time within rapid decay region (< 2 s) were linear with varying slopes (Fig. 5.5b). The rate constant was determined using the Eqn. 5.11.

$$\frac{I_{cat}}{I_{buf}} = \gamma^{\frac{1}{2}}\pi^{\frac{1}{2}} = \pi^{\frac{1}{2}}(kCt)^{\frac{1}{2}} \qquad (5.11)$$

where I_{cat} and I_{buf} currents on the modified electrodes in the presence and absence of hydrazine, k is the catalytic rate constant, C is the bulk concentration of hydrazine, and t the time elapsed in seconds. The slopes for the plots of I_{cat}/I_{buf} vs. square root of time were plotted

against concentration of hydrazine Fig. 5.5c. The slope is equal to πk where k is rate constant. The linear relationships of the plots in Fig. 5.5c are represented by equation 5.12 a-i.

1-H_2

$y = 58.74\ [N_2H_4]\ (\frac{s^{-1}}{mM}) + 10.816s^{-1}$, $R^2 = 0.95585$ 5.12a

1-Mn

$y = 575.13\ [N_2H_4]\ (\frac{s^{-1}}{mM}) + 338.44s^{-1}$, $R^2 = 0.9788$ 5.12b

GQDs

$y = 188.22\ [N_2H_4]\ (\frac{s^{-1}}{mM}) + 12.729s^{-1}$, $R^2 = 0.8364$ 5.12c

1-Mn@GQDs

$y = 1369.1\ [N_2H_4]\ (\frac{s^{-1}}{mM}) - 222.66s^{-1}$, $R^2 = 0.9742$ 5.12d

1-Mn--GQDs

$y = 608.66\ [N_2H_4]\ (\frac{s^{-1}}{mM}) + 434.49s^{-1}$, $R^2 = 0.8605$ 5.12e

2-Co

$y = 826.17\ [N_2H_4]\ (\frac{s^{-1}}{mM}) + 344.34s^{-1}$, $R^2 = 0.9681$ 5.12f

2-Co--GQDs

$y = 2006.6\ [N_2H_4]\ (\frac{s^{-1}}{mM}) + 740.65s^{-1}$, $R^2 = 0.9509$ 5.12g

2-Mn

$y = 153.77\ [N_2H_4]\ (\frac{s^{-1}}{mM}) + 45.661s^{-1}$, $R^2 = 0.9497$ 5.12h

2-Mn--GQDs

$y = 257.08\ [N_2H_4]\ (\frac{s^{-1}}{mM}) + 18.563s^{-1}$, $R^2 = 0.9382$ 5.12i

The catalytic rate constants for complexes **1** follow the order $4.36 \times 10^2 > 1.94 \times 10^2 > 1.83 \times 10^2 > 5.99 \times 10^1 > 1.87 \times 10^1$ for **1**-Mn@GQDs, **1**-Mn--GQDs, **1**-Mn**,** GQDs and **1**-H_2 respectively Table 5.1. **1**-Mn@GQDs showed the highest catalytic rate constant followed by **1**-Mn--GQDs. Although **1**-Mn--GQDs showed slightly better charge transfer in term of peak separation ΔE_p, Rct, and surface coverage, **1**-Mn@GQDs gave a higher rate constant for hydrazine oxidation. It is important to note that electrocatalytic activity does not only depend on the charge transfer, the mode of interaction of the analyte with the electrode also influences electrocatalytic activity. The catalytic rate constants of **1**-Mn--GQDs and **1**-Mn@GQDs were higher than that of **1**-Mn because of the effects of GQDs. The central metal introduction is also reported to improve the catalytic rate [31]. The higher catalytic rate constant for **1**-Mn@GQDs compared to **1**-Mn--GQDs, could be due to the covalent linkage of the amino group of the porphyrin and the carboxylic group of the quantum dots. Such covalent bonding improves the sharing of the π electron system of **1**-Mn and GQDs. **1**-H_2 performed the worst. For complexes **2**, **2**-Co--GQDs showed the highest catalytic rate constant followed by **2**-Co. In addition the introduction of GQDs improved the catalytic rate constant as expected. The **2**-Mn--GQDs showed higher catalytic rate constant than **2**-Mn but still lower when compared to **2**-Co alone. Rate constants are higher for complex **1**-Mn than **2**-Mn and **1**-Mn--GQDs than **2**-Mn--GQDs, this could be due to the high electron transfer resistance in **2**-Mn compared to **1**-Mn.

The limit of detection (LoD) for the detection of hydrazine using the modified electrodes (insert in Fig. 5.5a) was calculated by using Eqn.5.13.

$$LoD = \frac{3\sigma}{slope} \qquad (5.13)$$

where σ represents the standard deviation.

The LoD for complexes **1** was found to be 0.0023 mM < 0.0042 mM < 0.011 mM < 0.017 mM < 0.018 mM for **1**-Mn@GQDs, **1**-Mn--GQDs, **1**-Mn, **1**-H_2, and GQDs as shown in Table 5.1. The **1**-Mn@GQDs showed the lowest LoD. Of complexes **1**, the second lowest LoD was obtained from **1**-Mn--GQDs which could be caused by the π-π interaction between GQDs and the porphyrin. **1**-Mn also showed better LoD compared to **1**-H_2 and this could be due to the effect

of manganese as a central metal. The detection limits obtained in this study are lower than the values previously reported in some cases [26,97,98], Table 5.1.

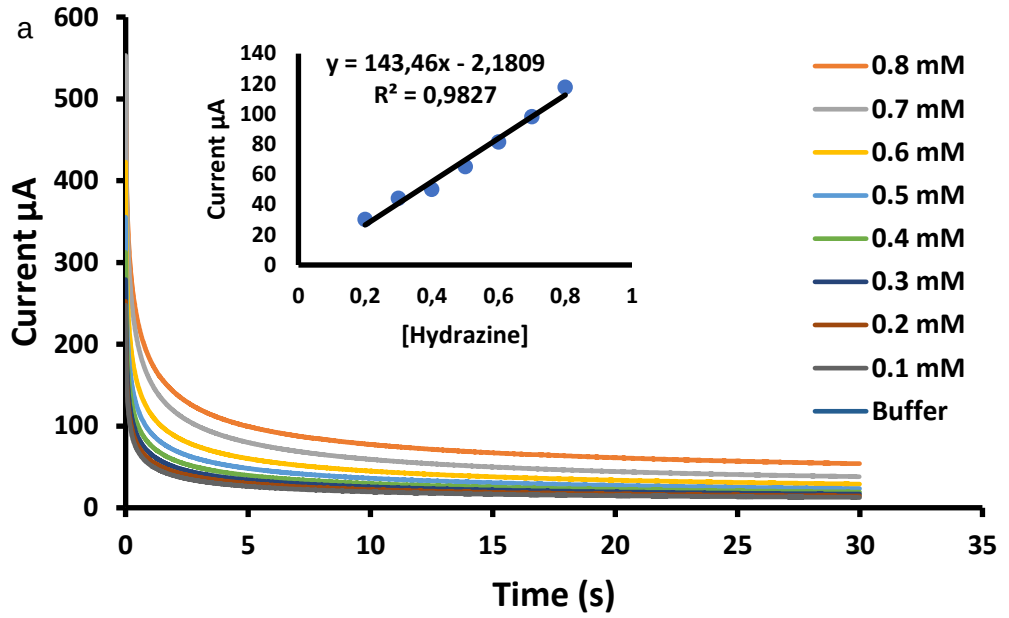

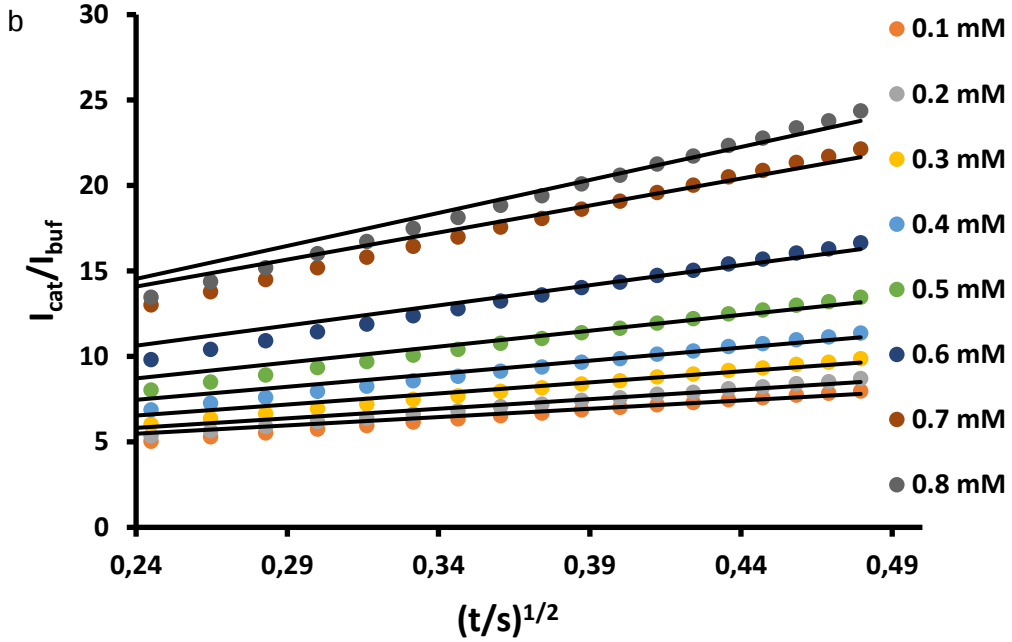

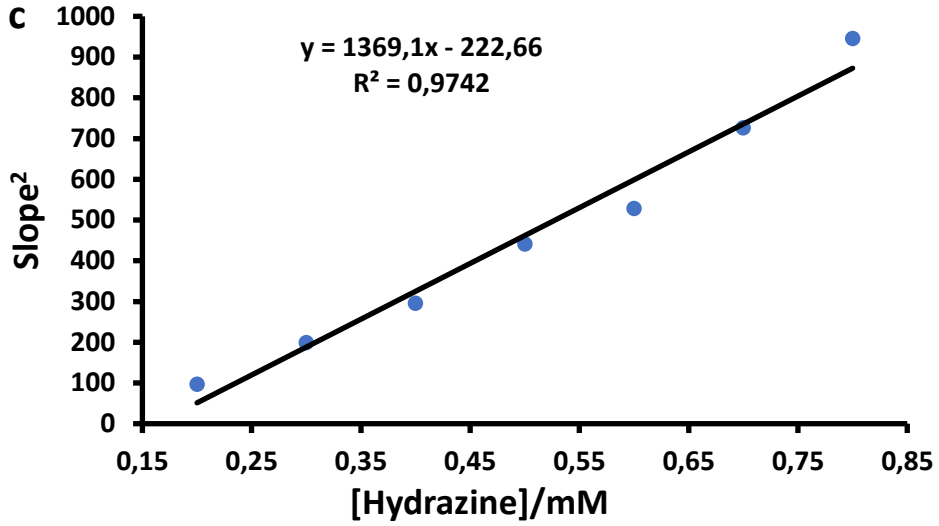

Fig. 5.5. a) Shows plot of chronoamperomegrams at different concentrations, insert = plot of Current vs. hydrazine concentration b) I_{cat}/I_{buff} vs. $t^{1/2}$ of **1**-Mn@GQDs and c) $Slope^2$ vs. hydrazine concentration.

5.4 Interference studies

Ammonia (0.1 mM) and aniline (0.1 mM) were explored as potential interfering analytes in the presence of hydrazine (0.025 mM) in the potential rage 0-1 V using square wave voltammogram (Fig. 5.6) using **1**-Mn@GQDs as an example. These compounds have a potential to interfere with hydrazine [99]. Interestingly there was no response found in ammonia, however aniline showed a response at 0.55 V. In the presence of ammonia, there was an 8.42% increase in the current for hydrazine oxidation and a small shift towards the positive potentials. A decrease of 13.54% was observed for hydrazine peak in the presence of aniline and a very small shift towards the positive potentials. However, a decrease of 42.61% was observed in the presence of all analytes and a small shift towards the positive potentials. Moreover, in the presence of aniline and in the mixture of all analytes, the sensor was able to show two separate responses for hydrazine and aniline at different potentials. These results showed that although the current is significantly affected by the presence of the interfering analytes used here, the sensor is still selective and specific.

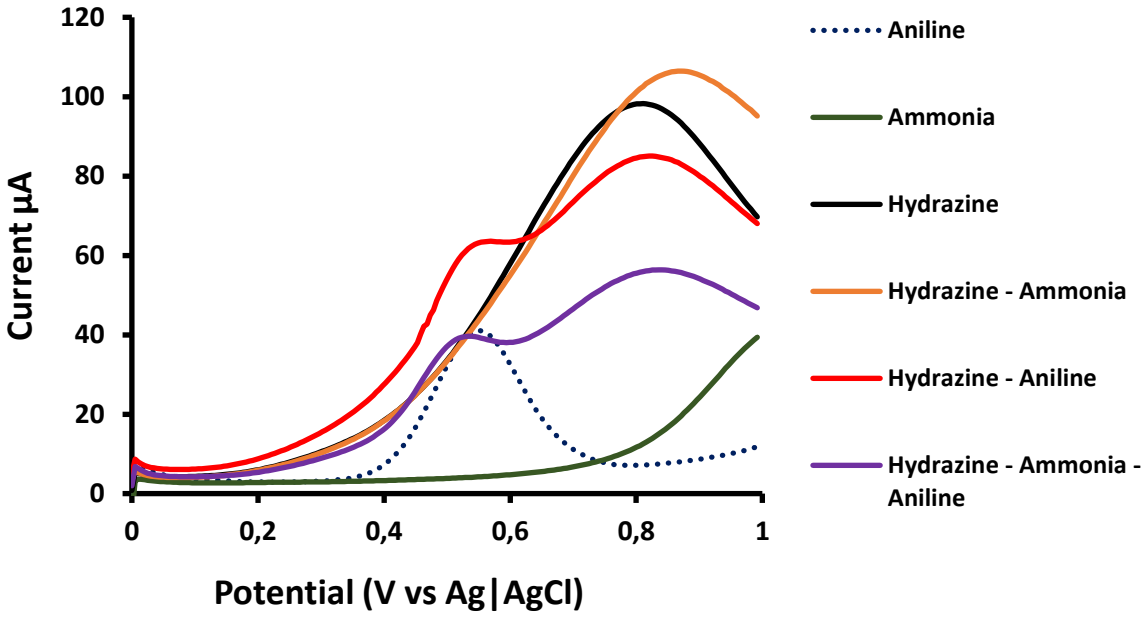

Fig. 5.6. Square wave voltammograms of **1**-Mn@GQDs for hydrazine alone, interferents alone and hydrazine in the presence of interferents. Concentrations: 0.1 mM aniline, 0.1 mM ammonia, 0.025 mM hydrazine.

5.5 Summary

The results discussed in this chapter showed the success of electrocatalytic oxidation of hydrazine with porphyrin alone, GQDs alone and their combination. As expected the introduction of GQDs to porphyrin improved the electrocatalytic activity. The presence of push-pull substituents on the porphyrin also play an important part on the catalysis which reduced the oxidation potential. Furthermore, no hydrogen formation was observed as there was no bubble formation during the oxidation of hydrazine experiment. This is an indication that there is no hydrolysis of hydrazine and therefore no loss in power.

Chapter 6:

Conclusions and Future aspects

6. Conclusions

The synthesis of symmetric and asymmetric porphyrins, GQDs and their composites was achieved and characterized using various spectroscopic characterization techniques. The electrochemical behavior towards hydrazine was tested and the following conclusion were made:

1. Complex **1**-H_2 and **1**-Mn are tetra amino substituted complexes. Complex **1**-Mn showed better catalytic activity compared to complex **1**-H_2. This due to the presence of manganese which enhanced the activity.
2. When complex **1**-Mn was linked to GQDs to produce complex **1**-Mn--GQDs and **1**-Mn@GQDs, the activity improved even further indicating that GQDs improves catalytic activity. Complex **1**-Mn@GQDs showed lower catalytic activity and LoD compared to **1**-Mn--GQDs. Surprisingly complex **1**-Mn showed lower oxidation peak potential when compared to the both composites.
3. In the case of complex **2**-Mn and **2**-Co which are contain push-pull substituents (3-amino and 1- carboxy), complex **2**-Co showed better catalytic properties in terms of catalytic rate constants and LoD. However, **2**-Mn showed better oxidation peak potential compared to **2**-Co. Moreover, complex **2**-Mn oxidize hydrazine at lower potentials compared to **1**-Mn amid to the presence of push-pull substituents.
4. The presence of GQDs resulted to the formation of complex **2**-Mn--GQDs and **2**-Co--GQDs. This improved the catalytic activity of both composites. Complex **2**-Co--GQDs showed better catalytic activity in terms of catalytic rate and LoD however complex **2**-Mn--GQDs showed lower oxidation peak potential compared to **2**-Co--GQDs. It is noted that for **1**-Mn after introducing GQDs the oxidation peak potential became larger. This could be due to the aggregation of GQDs hence the negative effect on the oxidation potential.
5. Of all the porphyrin-GQDs composites, **2**-Co--GQDs showed the highest catalytic rate followed by **1**-@Mn--GQDs with the lowest LoD. **2**-Mn--GQDs showed lower oxidation peak potential but lower catalytic rate when compared to **1**-Mn--GQDs due to aggregation.
6. The sensor showed good selectivity in the presence of interfering analytes. All probes showed good stability.

6.1 Future aspects

This work is evident that metal porphyrins are essential for hydrazine detection. However, an understanding of the structure and substituents and the understanding of nanomaterial could bring fantastic results in the field of electrocatalysis. The addition of GQDs to Mn porphyrins seem to negatively affect the oxidation potential for hydrazine oxidation and therefore it would be of interest to determine the electro-oxidation of hydrazine using combination of functionalized GQDs and porphyrin.

References

1) S. Hiroto, Y. Miyake, and H. Shinokubo, Synthesis and functionalization of porphyrins through organometallic methodologies. Chem. Rev. 2017, 117, 2910-3043.
2) M. da GH Vicente, and K. Smith, Syntheses and functionalizations of porphyrin macrocycles. Curr. Org. Synth. 2014, 11, 3-28.
3) A.D. Adler, F.R. Longo, and W. Shergalis, Mechanistic investigations of porphyrin syntheses. I. Preliminary studies on ms-tetraphenylporphin. J. Am. Chem. Soc. 1964, 86, 3145-3149.
4) J.C.A. Chaves, C.G. dos Santos, E.G.A de Miranda, J.T.A. Junior, and I.L Nantes, Phthal ocyanines and Some Current Applications, (editor; Y. Yilmaz), London, IntechOpen, Chapter 1, 2017, 1-28.
5) X. Lu, S. Devaramani, Electrochemical Investigation of Porphyrin and Its Derivatives a t Various Interfaces. Phthalocyanines and Some Current Applications, (editor; Y. Yilm az), London, IntechOpen, Chapter 3, 2017, 43-62.
6) O. Machold, U.W. and Stephan, The function of iron in porphyrin and chlorophyll biosynthesis. Phytochemistry, 1969, 8, 2189-2192
7) K.M Smith, Strategies for the synthesis of octaalkylporphyrin systems. The porphyrin handbook, editor (K.M Kadish and R. Guilard), Califonia, Academic Press, 2000, 1, 1-43.
8) P. Rothemund, and A.R. Menotti, Porphyrin Studies. IV. 1 The Synthesis of α, β, γ, δ-Tetraphenylporphine. J. Am. Chem. Soc. 1941, 63, 267-270.
9) J.S. Lindsey, The synthesis of meso-substituted porphyrins. In Metalloporphyrins Catalyzed Oxidations, Springer, Dordrecht, 1994, 49-86.
10) R. Lucas, J. Vergnaud, K. Teste, R. Zerrouki, V. Sol, and P. Krausz, A facile and rapid iodine-catalyzed meso-tetraphenylporphyrin synthesis using microwave activation. Tetrahedron Lett. 2008, 49, 5537-5539.
11) R. Giovannetti, The use of spectrophotometry UV-Vis for the study of porphyrins. Macro to nano spectroscopy, Rijeka, InTech, (editor; J. Uddin), 2012, 87-108.
12) S. Licoccia, M.L. Di Vona, and R. Paolesse, Acid-catalyzed cyclization of 1, 19-unsubstituted a, c-biladienes. J. Org. Chem. 1998, 63, 3190-3195.

13) Q. Yang, K.K. Streb, and B. Borhan, Polymer-supported synthesis of mono-substituted porphyrins. Tetrahedron Lett. 2005, 46, 6737-6740.

14) M. J. Stillman, T. Nyokong, Properties and Applications, In Phthalocyanines. (Editors; C. C. Leznoff, A. B. P. Lever), VCH, New York. 1989, vol 1.

15) M. Ptaszek, Rational design of fluorophores for in vivo applications. Prog Mol Biol Transl Sci. 2013, 113, 59-108.

16) M, Ghosh, A.K. Mora, S. Nath, A.K. Chandra, A. Hajra, and S. Sinha, Photophysics of Soret-excited free base tetraphenylporphyrin and its zinc analog in solution. Spectrochim. Acta A Mol. Biomol. Spectrosc. 2013, 116, 466-472.

17) L.F. Novaes, J. Liu, Y. Shen, L. Lu, J.M. Meinhardt, and S. Lin, Electrocatalysis as an enabling technology for organic synthesis. Chem. Soc. Rev, 2021, 50, 7941-8002.

18) A.J. Appleby, 1983. Electrocatalysis. In Comprehensive treatise of electrochemistry, Springer, Boston MA, 1983, 173-239.

19) R. Li, and C. Li, Photocatalytic water splitting on semiconductor-based photocatalysts. In Advances in catalysis. Dalian, Academic Press, 2017, 60, 1-57.

20) A.J. Bard, "Chemical modification of electrodes, J. Chem. Educ. 1983, 60, 301-304

21) T. Nyokong, Electrodes modified with monomeric M-N4 catalysts for the detection of environmentally important molecules, in: J.H. Zagal, F. Bedioui, J.-P. Dodelet (Eds.), N4-Macrocyclic Metal Complexes, Springer, USA, 2006, 315-361.

22) Z. Kamal, M.Z. Ghobadi, M.S. Mohseni, and H. Ghourchian. High-performance porphyrin-like graphene quantum dots for immuno-sensing of Salmonella typhi. *Biosens. Bioelectron*. 2021, *188*, 113334.

23) D.A. Offord, S.B. Sachs, M.S. Ennis, T.A. Eberspacher, J.H. Griffin, C.E. Chidsey, and J.P. Collman, Synthesis and properties of metalloporphyrin monolayers and stacked multilayers bound to an electrode via site specific axial ligation to a self-assembled monolayer. J. Am. Chem. Soc. 1998, 120, 4478-4487.

24) S.H. Kazemi, B. Hosseinzadeh, and S. Zakavi, Electrochemical fabrication of conducting polymer of Ni-porphyrin as nano-structured electrocatalyst for hydrazine oxidation. Sens. Actuators B Chem. 2015, 210, 343-348.

25) M.S. Quintino, K. Araki, H.E. Toma, and L. Angnes, New hydrazine sensors based on electropolymerized meso-tetra (4-sulphonatephenyl) porphyrinate manganese (III)/silver nanomaterial. Talanta, 2008, 74, 730-735.

26) S.I. Yamazaki, T. Ioroi, K. Tanimoto, K. Yasuda, K. Asazawa, S. Yamaguchi, and H. Tanaka, Electrochemical oxidation of hydrazine derivatives by carbon-supported metalloporphyrins. J. Power Sources, 2012, 204, 79-84.

27) S.V. Guerra, C.R. Xavier, S. Nakagaki, and L.T. Kubota, Electrochemical behavior of copper porphyrin synthesized into zeolite cavity: a sensor for hydrazine. Electroanalysis, 1998, 10, 462-466.

28) W. Hou, H. Ji, and E. Wang, Amperometric flow-injection analysis of hydrazine by electrocatalytic oxidation at cobalt tetraphenylporphyrin modified electrode with heat treatment. Talanta, 1992, 39, 45-50.

29) C. Canales, L. Gidi, R. Arce, and G. Ramírez, Hydrazine electrooxidation mediated by transition metal octaethylporphyrin-modified electrodes. New J Chem. 2016, 40, 2806-2813.

30) K.I. Ozoemena, Anodic oxidation and amperometric sensing of hydrazine at a glassy carbon electrode modified with cobalt (II) phthalocyanine–cobalt (II) tetraphenylporphyrin (CoPc-(CoTPP) 4) supramolecular complex. Sensors, 2006, 6, 874-891.

31) D.W. Pang, B.H. Deng, Z.L. and Wang, Electrocatalysis of metalloporphyrins—Part 14. Electro-oxidation of hydrazine catalyzed by water-soluble tetrakis (4-trimethylammoniumphenyl) porphyrin and its cobalt complex. Electrochim. Acta. 1994, 39, 847-851.

32) P. Muthukumar, and S.A. John, Efficient oxidation of hydrazine using amine-functionalized cobalt and nickel porphyrin-modified electrodes. J Solid State Electrochem. 2014, 18, 2393-2400.

33) F. Tasca, F.J. Recio, R. Venegas, D.A. Geraldo, M. Sancy, and J.H. Zagal, Linear versus volcano correlations for the electrocatalytic oxidation of hydrazine on graphite electrodes modified with MN4 macrocyclic complexes. Electrochim. Acta, 2014, 140, 314-319.

34) Y.H. Yao, J. Li, L.F. Yuan, Z.Q. Zhang and F.X. Zhang, Novel porphyrin–Schiff base conjugates: synthesis, characterization and in vitro photodynamic activities. RSC Adv. 2016, 6, 45681-45688.

35) J. Zhu, Z. Tan, W. Yang, Synthesize Polymeric Manganese Porphyrin with CuI/N,N-Dimethyl Glycine Acid Catalytic System and High-Efficiency Aerobic Catalytic Oxidation of Cyclic Ketones, Macromol. Res. 2017, 25, 792-798.

36) S. Benítez-Martínez, and M. Valcárcel, Graphene quantum dots in analytical science. Trends Analyt Chem. 2015, 72, 93-113.

37) M. Bacon, S.J. Bradley, and T. Nann, Graphene quantum dots. Part. Part. Syst. Charact. 2014, 31, 415-428.

38) A. Ghaffarkhah, E. Hosseini, M. Kamkar, A.A. Sehat, S. Dordanihaghighi, A. Allahbakhsh, C. van der Kuur, and M. Arjmand. Synthesis, applications, and prospects of graphene quantum dots: a comprehensive review. Small, 2022, 18, 2102683.

39) E. Haque, J. Kim, V. Malgras, K.R. Reddy, A.C. Ward, J. You, Y. Bando, M.S.A. Hossain, and Y. Yamauchi, Recent advances in graphene quantum dots: synthesis, properties, and applications. Small Methods, 2018, 2, 10800050.

40) D. Pan, J. Zhang, Z. Li, and M. Wu, Hydrothermal route for cutting graphene sheets into blue-luminescent graphene quantum dots. Adv. Mater. 2010, 22, 734-738.

41) S. Zhu, J. Zhang, X. Liu, B. Li, X. Wang, S. Tang, Q. Meng, Y. Li, C. Shi, R. Hu, and B. Yang, Graphene quantum dots with controllable surface oxidation, tunable fluorescence and up-conversion emission. RSC Adv. 2012, 2, 2717-2720.

42) L. Tang, R. Ji, X. Cao, J. Lin, H. Jiang, X. Li, K.S. Teng, C.M. Luk, S. Zeng, J. Hao, and S.P. Lau, Deep ultraviolet photoluminescence of water-soluble self-passivated graphene quantum dots. ACS nano, 2012, 6, 5102-5110.

43) W. Chen, G. Lv, W. Hu, D. Li, S. Chen, and Z. Dai, Synthesis and applications of graphene quantum dots: a review. Nanotechnol Rev. 2018, 7, 157-185.

44) D.B. Shinde, and V.K. Pillai, Electrochemical preparation of luminescent graphene quantum dots from multiwalled carbon nanotubes. Eur. J. Chem., 2012, *18*, 12522-12528.

45) Yan, Xin, Xiao Cui, Binsong Li, and Liang-shi Li. "Large, solution-processable graphene quantum dots as light absorbers for photovoltaics." Nano Lett. 2010, 10, 1869-1873.

46) B.A. Al Jahdaly, M.F. Elsadek, B.M. Ahmed, M.F. Farahat, M.M. Taher, and A.M. Khalil, Outstanding graphene quantum dots from carbon source for biomedical and corrosion inhibition applications: a review. Sustainability, 2021, 13, 2127.

47) C. Zhao, X. Song, Y. Liu, Y. Fu, L. Ye, N. Wang, F. Wang, L. Li, M. Mohammadniaei, M. Zhang, and Q. Zhang, Synthesis of graphene quantum dots and their applications in drug delivery. J. Nanobiotechnology. 2020, 18, 1-32.

48) S. Gupta, T. Smith, A. Banaszak, and J. Boeckl, Graphene quantum dots electrochemistry and sensitive electrocatalytic glucose sensor development. Nanomaterials, 2017, 7, 301.

49) Y.R. Kumar, K. Deshmukh, K.k. Sadasivuni, and S.K. Pasha, Graphene quantum dot based material for sensing, bio-imaging and energy storage application: a review. RSC Advances. 2020, 10, 23861-23898.

50) S. Campuzano, P. Yáñez-Sedeño, and J.M. Pingarrón, Carbon dots and graphene quantum dots in electrochemical biosensing. Nanomaterials, 2019, 9, 634.

51) L. Zhang, D. Peng, R.P. Liang, J.D. and Qiu, Nitrogen-doped graphene quantum dots as a new catalyst accelerating the coordination reaction between cadmium (II) and 5, 10, 15, 20-tetrakis (1-methyl-4-pyridinio) porphyrin for cadmium (II) sensing. Anal. Chem. 2015, 87, 10894-10901.

52) S. Centane, and T. Nyokong, The antibody assisted detection of HER2 on a cobalt porphyrin binuclear framework and gold functionalized graphene quantum dots modified electrode. J. Electroanal. Chem. 2021, 880, 114908.

53) M. Managa, O.J. Achadu, and T. Nyokong, Photophysical studies of graphene quantum dots-Pyrene-derivatized porphyrins conjugates when encapsulated within Pluronic F127 micelles. Dyes Pigm. 2018, 148, 405-416.

54) G. Xue, S. Yu, Z. Qiang, L. Xiuying, and L. Jiangrong, Application of maleimide modified graphene quantum dots and porphyrin fluorescence resonance energy transfer in the design of ‘‘turn-on’’fluorescence sensors for biothiols. Anal. Chim. Acta. 2020, 1108, 46-53.

55) A. Pallikkara, D. Sebastian, and K. Ramakrishnan, An Investigation on the Effect of Extended Conjugation on the Photophysical Properties of Graphene Quantum Dot-Porphyrin Dyads. Chemistry Select. 2021, 6, 12224-12232.

56) Y. Cao, H. Dong, Z. Yang, X. Zhong, Y. Chen, W. Dai, and X. Zhang, Aptamer-conjugated graphene quantum dots/porphyrin derivative theranostic agent for intracellular cancer-related microRNA detection and fluorescence-guided photothermal/photodynamic synergetic therapy. ACS Appl. Mater. Interfaces. 2017, 9, 159-166.

57) M. Mahyari, and J. Nasrollah Gavgani, Cobalt porphyrin supported on N and P co-doped graphene quantum dots/graphene as an efficient photocatalyst for aerobic oxidation of alcohols under visible-light irradiation. Res. Chem. Intermed. 2018, 44, 3641-3657.

58) H.N. Nguyen MC USAF, J.A. Chenoweth, V.S. Bebarta MC USAF, T.E. Albertson, and C.D. Nowadly MC USAF, The toxicity, pathophysiology, and treatment of acute hydrazine propellant exposure: a systematic review. Mil. Med. 2021, 186, 319-326.

59) I. Kang, W.S. Shin, S. Manivannan, Y. Seo, and K. Kim, An electrochemical sensor for hydrazine based on in situ grown cobalt hexacyanoferrate nanostructured film. J. Electrochem. Sci. Technol. 2016, 7, 277-285.

60) O.J. Achadu, T. Nyokong, Interaction of graphene quantum dots with 4-acetamido-2, 2, 6, 6-tetramethylpiperidine-oxyl free radicals: A spectroscopic and fluorimetric study, J. Fluoresc. 2016, 26, 283-295.

61) J. Shi, C. Chan, Y. Pang, W. Ye, F. Tian, J. Lyu, Y. Zhang, and M. Yang, A fluorescence resonance energy transfer (FRET) biosensor based on graphene quantum dots (GQDs) and gold nanoparticles (AuNPs) for the detection of mecA gene sequence of Staphylococcus aureus. Biosens. Bioelectron. 2015, 67, 595-600.

62) S. Centane, O.J. Achadu, T. Nyokong, Effects of substituents on the electrocatalytic activity of cobalt phthalocyanines when conjugated to graphene quantum dots, Electroanalysis. 2017, 29, 2470-2482.

63) M.G. Ribeiro, and G.C. Azzellini, Synthesis of new cationic metalloporphyrins and heterodimer formation with anionic metallophthalocyanines. J. Braz. Chem. Soc. 2003, 14, 914-921.

64) V.A. Chhabra, R. Kaur, N. Kumar, A. Deep, C. Rajesh, and K.H. Kim, 2018. Synthesis and spectroscopic studies of functionalized graphene quantum dots with diverse fluorescence characteristics. RSC Adv, 2018, 8, 11446-11454.

65) S. Belali, A.R. Karimi, M. Hadizadeh, Cell-specific and pH-sensitive nanostructure hydrogel based on chitosan as a photosensitizer carrier for selective photodynamic therapy. Int. J. Biol. Macromol. 2018, 110, 437-448.

66) X. Cai, Y. Zhang, X. Zhang, J. Jiang, Structures and properties of 2, 3, 9, 10, 16, 17, 23, 24-octasubstituted phthalocyaninato-lead complexes: the substitutional effect study on the basis of density functional theory calculations. J. Mol. Struct. 2006, 801, 71-80.

67) E. Fagadar-Cosma, M. C. Mirica, I. Balcu, C. Bucovicean, C. Cretu, I. Armeanu, G.Fagadar-Cosma, Syntheses, spectroscopic and AFM characterization of some manganese porphyrins and their hybrid silica nanomaterials, Molecules. 2009, 14, 1370-1388.

68) X. Gao, B. Zhang, Q. Zhang, Y. Tang, X. Liu, J. Li, The influence of combination mode on the structure and properties of graphene quantum dot-porphyrin composites. Colloids Surf. B. 2018, 172, 207-212.

69) M.H.V. Reddy, R.M. Al-Shammari, N. Al-Attar, S. Lopez, T.E. Keyes, J.H. Rice, Optical properties of porphyrin – graphene oxide composites, Proc. SPIE. 2014, 9172, 91720–91727.

70) P. Linkov, M. Artemyev, A.E. Efimov, I. Nabiev, Comparative advantages and limitations of the basic metrology methods applied to the characterization of nanomaterials. Nanoscale, 2013, 5, 8781-8798.

71) T. Souza, V. Ciminelli, N. Mohallem, A comparison of TEM and DLS methods to characterize size distribution of ceramic nanoparticles. J. Phys. Conf. Ser. 2016, 733, 12039-12044.

72) J. B. Lambert, H. F. Shurvell, D. A. Lightner, R. G. Cooks, Introduction to Organic Spectroscopy, New York, Macmillan, 1987.

73) H. Abudukeremu, N. Kari, Y. Zhang, J. Wang, P. Nizamidin, Sh. Abliz, A. Yimit, Highly sensitive free-base-porphyrin-based thin-film optical waveguide sensor for detection of low concentration NO 2 gas at ambient temperature, J. Mater. Sci. 2018, 53, 10822–10834.

74) G. Lu, X. Zhang, X. Cai, J. Jiang, Tuning the morphology of self-assembled nanostructures of amphiphilic tetra (p-hydroxyphenyl) porphyrins with hydrogen

bonding and metal–ligand coordination bonding. J. Mater. Chem. 2019, 19, 2417-2424.

75) B. Babu, E. Amuhaya, D. Oluwole, E. Prinsloo, J. Mack, T. Nyokong, Preparation of NIR absorbing axial substituted tin (iv) porphyrins and their photocytotoxic properties. MedChemComm, 2019, 10, 41-48.

76) X. Li, A. Liu, D. Chu, C. Zhang, Y. Du, J. Huang, P. Yang, High performance of manganese porphyrin sensitized p-Type CuFe2O4 photocathode for solar water splitting to produce hydrogen in a tandem photoelectrochemical cell. Catalysts, 2018, 8, 108.

77) M.N. Biyareh, A.R. Rezvani, K. Dashtian, M. Montazerozohori, M. Ghaedi, A.M. Asl, and J. White. Potentiometric ion-selective electrode based on a new single crystal cadmium (II) schiff base complex for detection of fluoride ion: Central composite design optimization. *IEEE Sens.* 2018, *19*, 413-425.

78) F.J Rawson, A.J. Downard and K.H. Baronian, Electrochemical detection of intracellular and cell membrane redox systems in Saccharomyces cerevisiae, Sci. Rep. 2014, 4, 1-9.

79) D.O. Oluwole, and T. Nyokong, Physicochemical behavior of nanohybrids of mono and tetra substituted carboxyphenoxy phthalocyanine covalently linked to GSH–CdTe/CdS/ZnS quantum dots. Polyhedron, 2015, 87, pp.8-16.

80) I. Sebarchievici, B.O. Tăranu, M. Birdeanu, S.F. Rus, and E. Fagadar-Cosma, Electrocatalytic behaviour and application of manganese porphyrin/gold nanoparticle-surface modified glassy carbon electrodes. Appl. Surf. 2016, 390, 131-140.

81) J.J. Gooding, V.G. Praig, E. a Hall, Platinum-catalyzed enzyme electrodes immobilized on gold using self-assembled layers, Anal. Chem. 1998, 70, 2396–2402.

82) E. Mark, T. Orazem, Electrochemical Impedance Spectroscopy, New York, John Wiley & Sons, 2008, 383-389.

83) G. M. Ucoski, S.Nakagaki, F. S. Nunes, Electrochemistry and spectroelectrochemistry of 5,10,15,20-tetrakis(1,3-benzodioxole) porphyrin and its manganese and iron complexes, J. Porphyr. Phthalocyanines. 2014, 18, 1093–1100.

84) O. Ramirez-Gutierrez, J. Claret, J. M. Ribo, Cyclic voltammetry of water-soluble manganese porphyrins in the presence of cyclodextrins, J. Porphyr. Phthalocyanines. 2005, 9, 368-376.

85) N. Hashemzadeh, M. Hasanzadeh, N. Shadjou, J. Eivazi-Ziaei, M. Khoubnasabjafari, A. Jouyban, Graphene quantum dot modified glassy carbon electrode for the determination of doxorubicin hydrochloride in human plasma, J. Pharmaceut. Anal. 2016, 6, 235–241.

86) J.H. Zagal, S. Lira, S. Ureta-Zañartu, A mechanistic study of the electro-oxidation of hydrazine on phthalocyanines of VO, Cr, Mn, Ni, Cu and Zn attached to graphite electrodes, J. Electroanal. Chem. Interf. Electrochem. 1986, 210, 95-110.

87) I.G. Casella, M. Contursi, Electrocatalytic Oxidation of Some Hydrazine Compounds at Glassy Carbon Electrode Modified with Co-Gluconate Complex, Electroanalysis. 2012, 24, 752-758.

88) D.W. Pang, Z.L. Wang, C.S. Cha, Electrocatalysis of metalloporphyrins—Part 11. Catalytic electroreduction of dithiodipropionic acid with water-soluble cobalt tetrakis (4-trimethylammoniumphenyl) porphyrin catalyst, Electrochim. Acta. 1992, 37, 2591-2594.

89) F. Tan, L. Cong, X. Li, Q. Zhao, H. Zhao, X. Quan, J. Chen, An electrochemical sensor based on molecularly imprinted polypyrrole/graphene quantum dots composite for detection of bisphenol A in water samples, Sens. Actuators, B. 2016, 233, 599-606.

90) D.A. Venegas-Yazigi, G.I. Cárdenas-Jirón, and J.H. Zagal, Theoretical study of the electron transfer reaction of hydrazine with cobalt (II) phthalocyanine and substituted cobalt (II) phthalocyanines. J. Coord. Chem. 2003, 56, 1269-1275.

91) F.S. Damos, R.D. Cássia Silva Luz, and A.A. Tanaka, Electroanalysis of Hydrazine and Related Compounds by Oxidation Promoted with MN4 Macrocyclics. In Electrochemistry of N4 Macrocyclic Metal Complexes, Springer, Cham. 2016, 201-223.

92) C. San Martín, P. Dreyse, C. García, K. Calfumán, D. Villagra, M. Isaacs, Electrochemical reduction of nitrite at polymeric Co (II)-tetra-3-amino-phenyl-porphyrin modified electrode, J. Chil. Chem. Soc. 2007, 52, 1305-1308.

93) A. Salimi, K. Abdi, Enhancement of the analytical properties and catalytic activity of a nickel hexacyanoferrate modified carbon ceramic electrode prepared by two-step sol–gel technique: application to amperometric detection of hydrazine and hydroxyl amine, Talanta. 2004, 63, 475-483.

94) C.A. Caro, F. Bedioui, J.H. Zagal, Electrocatalytic oxidation of nitrite on a vitreous carbon electrode modified with cobalt phthalocyanine, Electrochim. Acta. 2002, 47, 1489-1494.

95) A.S. Adekunle, K.I. Ozoemena, Electrocatalytic oxidation of diethylaminoethanethiol and hydrazine at single-walled carbon nanotubes modified with Prussian blue nanoparticles, Electroanalysis. 2010, 22, 2519–2528.

96) L.S. Mpeta, T. Nyokong, Electrocatalytic activity of ethynylbenzyl phthalocyanines when linked to quantum dots via click chemistry: Towards efficient oxygen reduction reaction and H_2O_2 oxidation. J. Electroanal. Chem. 2019, 840, 218-229.

97) S. Sakthinathan, S. Kubendhiran, S.M. Chen, P. Tamizhdurai, Reduced graphene oxide/gold tetraphenyl porphyrin (RGO/Au–TPP) nanocomposite as an ultrasensitive amperometric sensor for environmentally toxic hydrazine, RSC Adv. 2016, 6, 56375-56383.

98) M. Sarno, E. Ponticorvo, Metal–metal oxide nanostructure supported on graphene oxide as a multifunctional electro-catalyst for simultaneous detection of hydrazine and hydroxylamine, Electrochem. Commun. 2019, 107, 106510-106517.

99) A.N. Koreshkova, V. Gupta, A. Peristyy, P. N. Nesterenko, T. Rodemann, B. Paull, Ion chromatographic determination of hydrazine in excess ammonia for monitoring graphene oxide reduction reaction, Talanta. 2019, 205, 120081.

Appendices

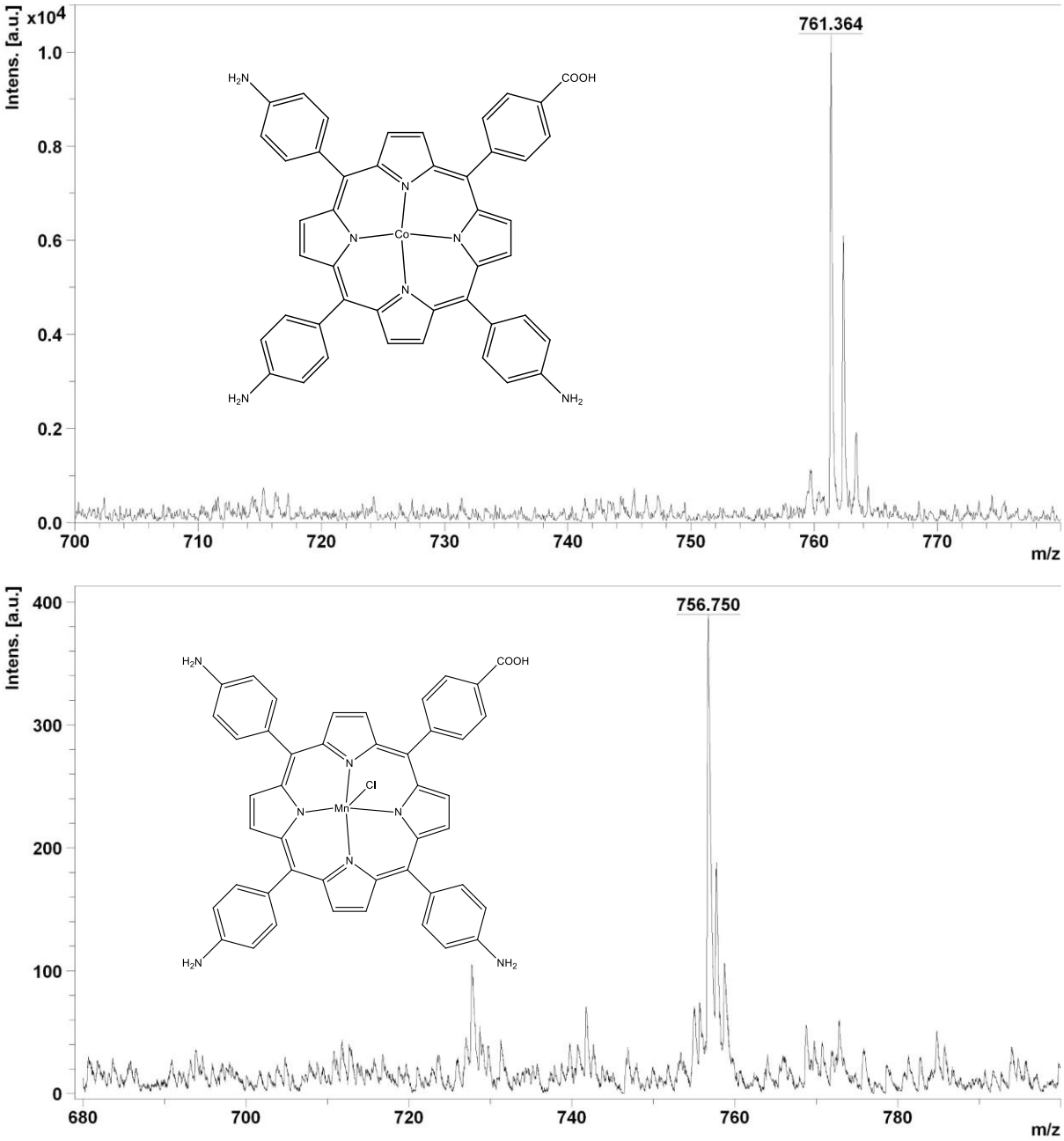

Fig A1. Mass spectra of **2**-Co and **2**-Mn.

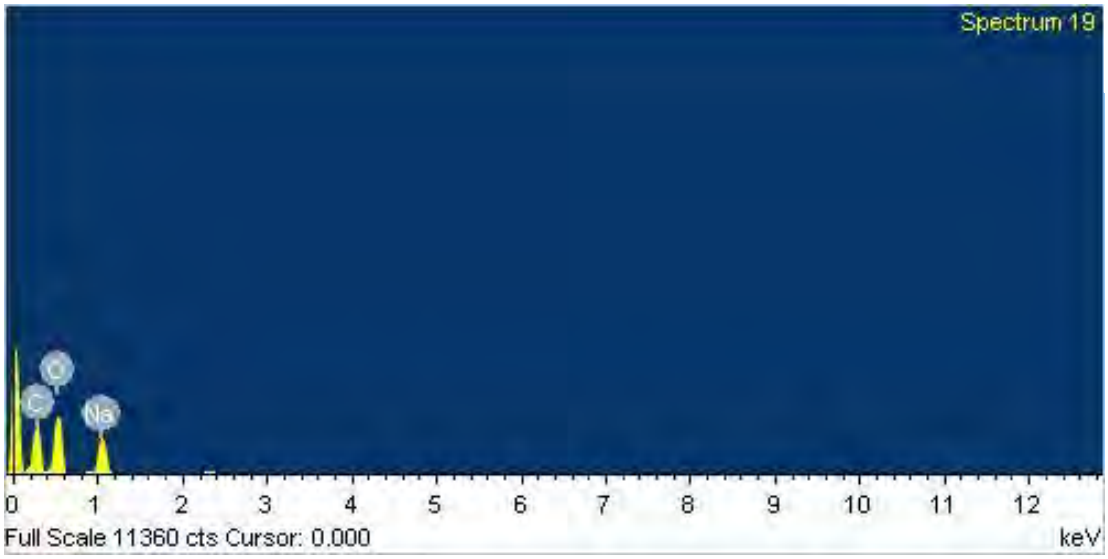
Spectrum 19
O
C
Na
0 1 2 3 4 5 6 7 8 9 10 11 12
Full Scale 11360 cts Cursor: 0.000
keV

(a)

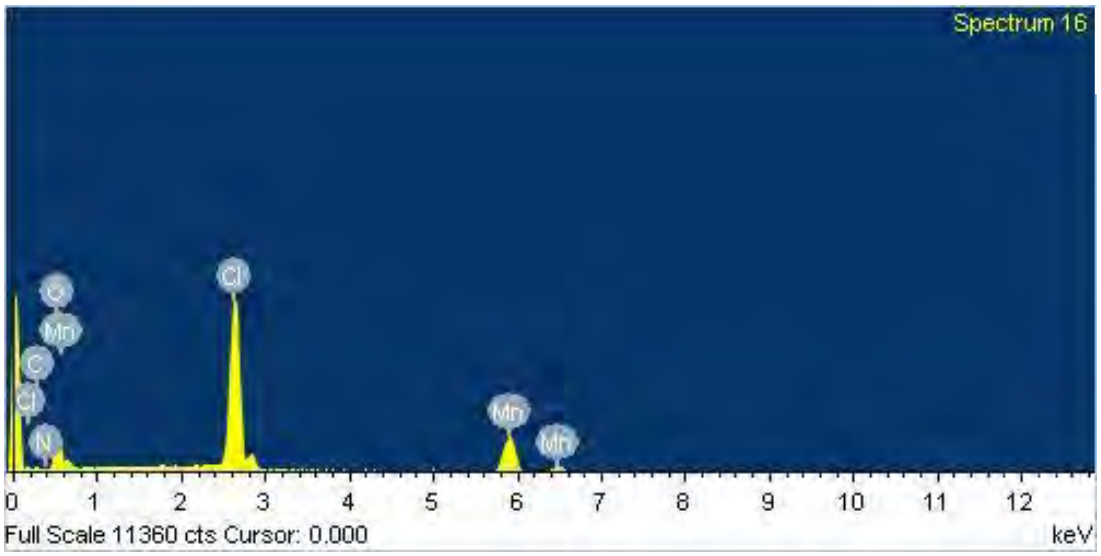
Spectrum 16
O
Mn
C
Cl
N
Cl
Mn
Mn
0 1 2 3 4 5 6 7 8 9 10 11 12
Full Scale 11360 cts Cursor: 0.000
keV

(b)

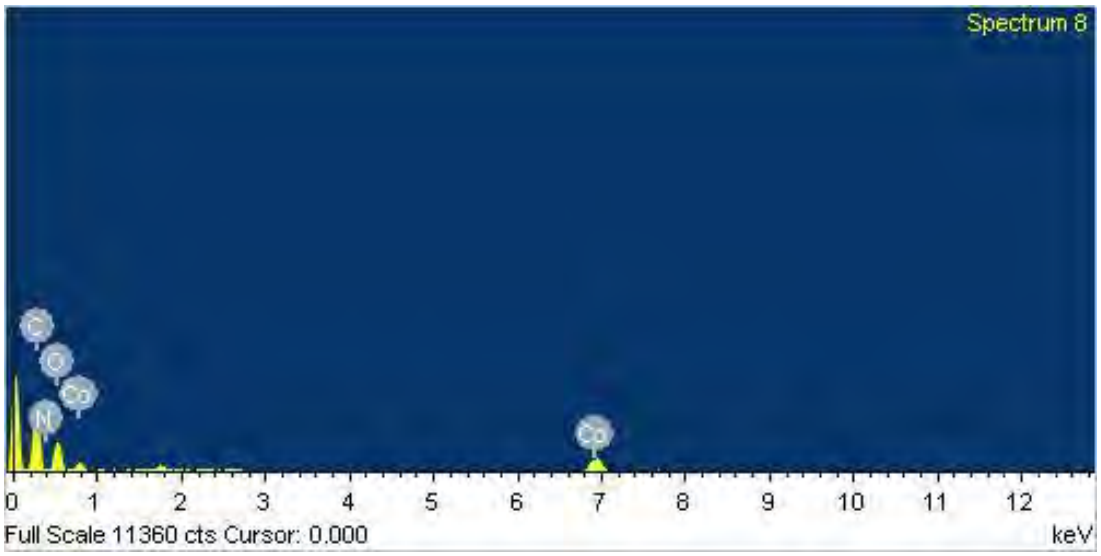
Spectrum 8
C
O
Co
N
Co
0 1 2 3 4 5 6 7 8 9 10 11 12
Full Scale 11360 cts Cursor: 0.000
keV

(c)

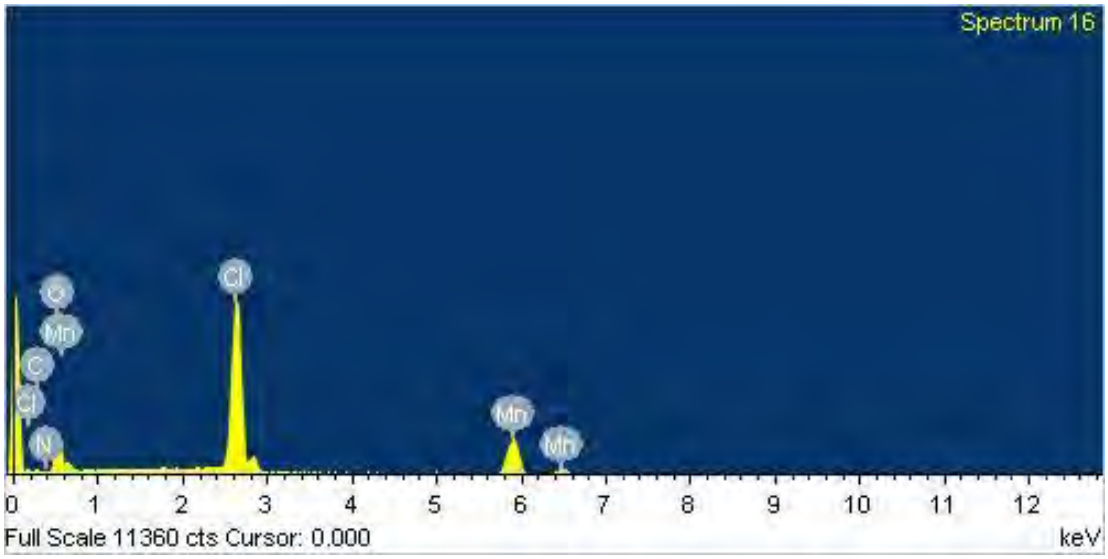

(d)

Fig A2. EDX pattern of (a) GQDs, (b) **2**-Mn, (c) **2**-Co--GQDs and (d) **2**-Mn--GQDs.

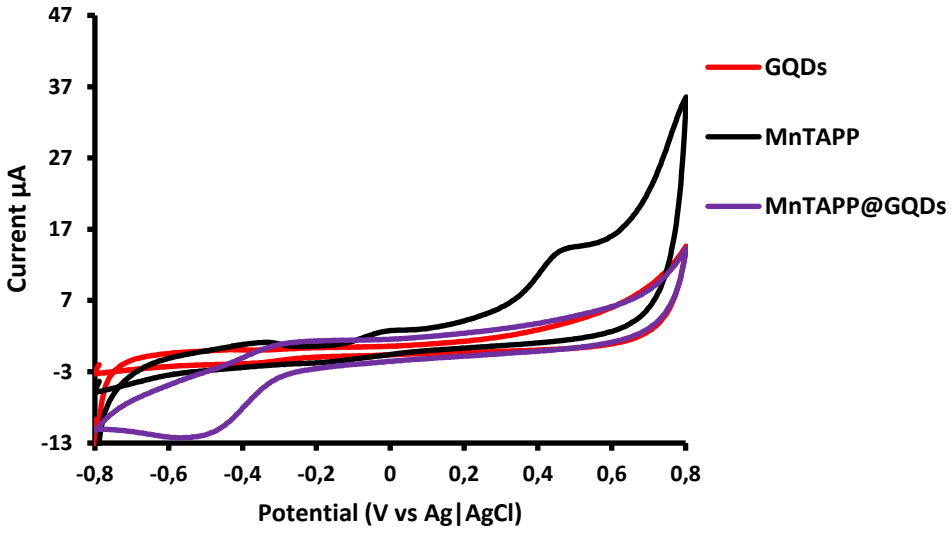

Fig A3. Cyclic Voltammograms of GQDs, **1**-Mn, and **1**-Mn@GQDs at 100 mV/s in 0.1 M NaOH.